Cell Reports

Article

A tripartite circRNA/mRNA/miRNA interaction regulates glutamatergic signaling in the mouse brain

Graphical abstract

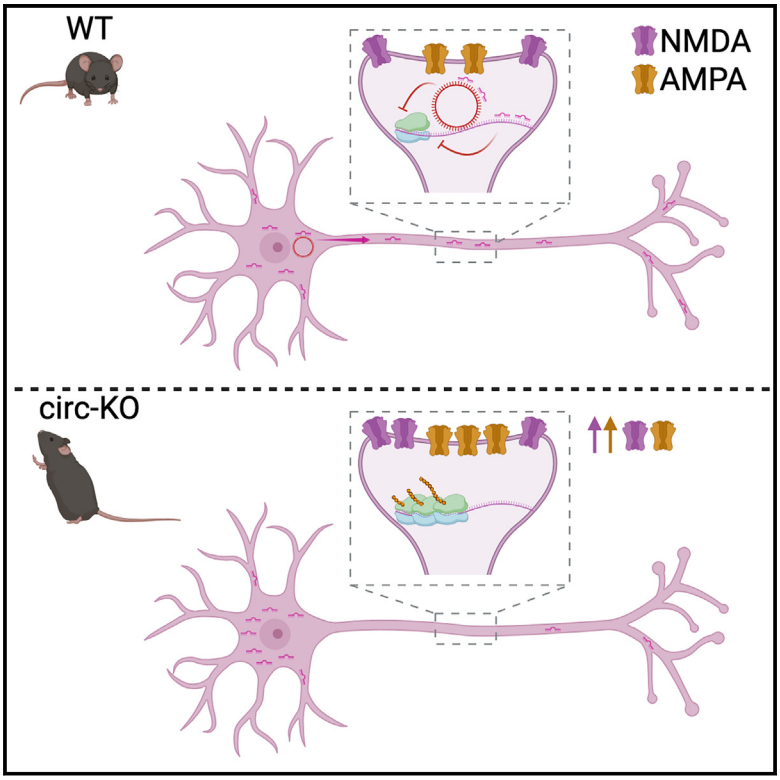

Authors

Valentina Silenzi, Eleonora D'Ambra, Tiziana Santini, ..., Elvira De Leonibus, Irene Bozzoni, Mariangela Morlando

Correspondence

irene.bozzoni@uniroma1.it (I.B.), mariangela.morlando@unipg.it (M.M.)

In brief

Silenzi et al. report that the loss of circDlc1(2) in a KO mouse model upregulates glutamatergic genes, enhances synaptic transmission, and causes hyperactivity. circDlc1(2) interacts with *gluRNA* and miR-130b-5p, synergizing with the latter to repress *gluRNA* expression. It also spatially controls miR-130b-5p localization, highlighting an unprecedented gene regulation mechanism.

Highlights

- KO mouse model reveals circDlc1(2) role in glutamatergic gene regulation and behavior
- Loss of circDlc1(2) enhances synaptic transmission, leading to hyperactivity in mice
- circDlc1(2) and miR-130b-5p interact and control gluRNA expression synergistically
- circDlc1(2) controls miR-130b-5p synaptic localization

Silenzi et al., 2024, Cell Reports *43*, 114766
October 22, 2024
https://doi.org/10.1016/j.celrep.2024.114766

CellPress

Cell Reports

CellPress
OPEN ACCESS

Article

A tripartite circRNA/mRNA/miRNA interaction regulates glutamatergic signaling in the mouse brain

Valentina Silenzi,[1,14] Eleonora D'Ambra,[1,2,14] Tiziana Santini,[1] Sara D'Uva,[1,2] Adriano Setti,[1] Nicolò Salvi,[1] Carmine Nicoletti,[3] Rebecca Scarfò,[1,13] Federica Cordella,[2,4] Brunella Mongiardi,[5,6] Diletta Cavezza,[5,6] Nara Liessi,[7] Laura Ferrucci,[4] Davide Ragozzino,[4,8] Andrea Armirotti,[7] Silvia Di Angelantonio,[2,4,9] Elvira De Leonibus,[6,10] Irene Bozzoni,[1,2,15,*] and Mariangela Morlando[11,12,*]

[1]Department of Biology and Biotechnologies "Charles Darwin", Sapienza University of Rome, 00185 Rome, Italy
[2]Center for Life Nano- & Neuro-Science@Sapienza of Istituto Italiano di Tecnologia (IIT), 00161 Rome, Italy
[3]Department of Anatomical, Histological, Forensic Medicine and Orthopedic Sciences, Section of Histology and Embryology, Sapienza University of Rome, 00161 Rome, Italy
[4]Department of Physiology and Pharmacology, Sapienza University of Rome, 00185 Rome, Italy
[5]Institute of Biochemistry and Cell Biology, CNR, Monterotondo, 00015 Rome, Italy
[6]Telethon Institute of Genetics and Medicine (TIGEM), Pozzuoli, 80078 Naples, Italy
[7]Analytical Chemistry Facility, Istituto Italiano di Tecnologia, Via Morego 30, 16163 Genova, Italy
[8]IRCCS Santa Lucia Foundation, 00179 Rome, Italy
[9]D-Tails srl BC, 00165 Rome, Italy
[10]Institute of Cellular Biology and Neurobiology "ABT", CNR, Monterotondo, 00015 Rome, Italy
[11]Department of Pharmaceutical Sciences, "Department of Excellence 2018-2022", University of Perugia, 06123 Perugia, Italy
[12]Present address: Department of Biology and Biotechnologies "Charles Darwin," Sapienza University of Rome, 00185 Rome, Italy
[13]Present address: Roche Innovation Center Zurich, Roche Pharma Research and Early Development, Zurich, Switzerland
[14]These authors contributed equally
[15]Lead contact
*Correspondence: irene.bozzoni@uniroma1.it (I.B.), mariangela.morlando@unipg.it (M.M.)
https://doi.org/10.1016/j.celrep.2024.114766

SUMMARY

Functional studies of circular RNAs (circRNAs) began quite recently, and few data exist on their function *in vivo*. Here, we have generated a knockout (KO) mouse model to study *circDlc1(2)*, a circRNA highly expressed in the prefrontal cortex and striatum. The loss of *circDlc1(2)* led to the upregulation of glutamatergic-response-associated genes in the striatal tissue, enhanced excitatory synaptic transmission in neuronal cultures, and hyperactivity and increased stereotypies in mice. Mechanistically, we found that *circDlc1(2)* physically interacts with some mRNAs, associated with glutamate receptor signaling (*gluRNA*s), and with miR-130b-5p, a translational regulator of these transcripts. Notably, differently from canonical microRNA (miRNA) "sponges," *circDlc1(2)* synergizes with miR-130b-5p to repress *gluRNA* expression. We found that *circDlc1(2)* is required to spatially control miR-130b-5p localization at synaptic regions where *gluRNA* is localized, indicating a different layer of regulation where circRNAs ensure robust control of gene expression via the correct subcellular compartmentalization of functionally linked interacting partners.

INTRODUCTION

Circular RNAs (circRNAs) are covalently closed circular molecules that arise from a back-splicing reaction.[1,2] They are evolutionarily conserved and increasingly recognized as important regulators of gene expression.[3]

Although circRNAs are expressed in all tissues, their expression is higher in the mammalian brain,[4–6] where they also show specific subcellular localization in neurites and synapses.[7,8] In the nervous system, their expression is associated with many functions, including neuronal activation and homeostatic plasticity, suggesting a crucial role in the complex molecular processes that underlie synaptic plasticity and learning.[7] Moreover, general insults to neurons or brain-related diseases have been also correlated with changes in circRNA expression.[9–11]

It is therefore not surprising that circRNAs appear to be involved in a variety of neuronal stress responses, and their abnormal expression or function may contribute to the onset, progression, and/or severity of various complex neurological disorders,[9,12] such as Parkinson's,[13,14] Alzheimer's,[15,16] and autism spectrum disorder.[17] In most of these cases, besides several studies indicating their role as microRNA (miRNA) "sponges,"[18] the molecular mechanism at the basis of their function has been largely unexplored. In this study, we

investigated the biological role and mechanism of action of circ-16[19] *in vivo*, here re-named *circDlc1(2)*, according to the new circRNA nomenclature.[20] Such circRNA, initially identified in *in-vitro*-derived motoneurons (MNs),[19,21] is now shown by *in vivo* studies to be highly enriched in the cortex and striatum. Accordingly, *circDlc1(2)* knockout (KO) mice show hyperactivity, increased stereotypies, and behavioral disinhibition associated with upregulated glutamatergic signaling and plasticity in cortico-striatal pathways. Glutamate, through ionotropic glutamate AMPA and NMDA receptors, regulates fronto-striatal excitability and plasticity that are crucial for the normal regulation of goal-directed behaviors.

Mechanistically, *circDlc1(2)* was found to physically interact with miR-130b-5p and control its localization at the neuron periphery; moreover, *circDlc1(2)* was discovered to bind several mRNAs, known to localize in synaptic regions,[22,23] which are involved in glutamatergic circuitries and found to be targets of miR-130b-5p. *circDlc1(2)* was shown to favor miR-130b-5p repression of target mRNAs, indicating a mechanism that is different from that of a canonical miRNA sponge and instead controls subcellular localization and promotes miRNA activity.

RESULTS

Generation of *circDlc1(2)* loss-of-function mouse model

Three major coding mRNA isoforms arise from the deleted in liver cancer (*Dlc1*) locus through the tissue-specific activation of three transcriptional start sites (*Dlc1-201*, *Dlc1-203*, and *Dlc1-206*)[24,25]; the three isoforms share the functional sequence encoding the Rho GTPase-activating protein (RhoGAP) in the C terminus. The second exon of the longest and least-characterized isoform of *Dlc1* transcript (*Dlc1-206*, ENSMUST00000163663.3) undergoes circularization, giving rise to *circDlc1(2)* (Figure 1A). A previous study from Errichelli et al.[19] showed that *circDlc1(2)* is upregulated during murine MN differentiation and conserved in human.[19,21]

With the aim of studying its role *in vivo*, we have initially tested its expression in different neuronal districts and found a 3-fold higher expression in the striatum and prefrontal cortex with respect to the spinal cord (Figure 1B). Fluorescence *in situ* hybridization (FISH) analysis was then performed on whole-brain cryosections (Figures 1C and S1), confirming that *circDlc1(2)* is abundantly expressed in the striatum and cortex, specifically in layers V and VI, where glutamatergic pyramidal neurons project to different neuronal structures, including the striatum.[26] We then generated a KO mouse model (circ-KO) by employing the CRISPR-Cas9 technology. Since the intronic regions flanking the circularizing exon should contain sequence elements promoting the back-splicing reaction, we decided to remove intron 1 of the *Dlc1-206* gene, as its length is much shorter than intron 2 (13,362 vs. 79,484 bp). To this end, a CRISPR approach was used with RNA guides targeting intron 1 in combination with a single-stranded DNA donor able to restore the exon 1-exon 2 junction (Figure 1D). This strategy was applied to avoid the loss of expression of the linear mRNA isoform (*lin-Dlc1*).

Mutant heterozygous *circDlc1(2)* founders displayed the predicted deletion of intron 1 together with the proper restoration of the exon 1-exon 2 junction (Figure S2A). The mutant founders were backcrossed with C57BL/6J and the progeny further crossed in order to get homozygous animals (circ-KO; Figures S2A and S2B). Quantitative real-time PCR (real-time qPCR) performed on total RNA derived from the striatum and cortex revealed a complete loss of *circDlc1(2)* expression in homozygous animals. In parallel, we found a decrease of the linear counterpart in the same brain regions (Figure S2C). However, real-time qPCR and sequencing data indicated that the two shorter isoforms (*Dlc1-201* and *Dlc1-203*), as well as all transcripts arising from 2 Mb *Dlc1*-surrounding regions, did not show any variation in the striatum and cortex of *circDlc1(2)* KO mice (Figure S2C; data not shown). These findings indicate that the genetic editing performed on *lin-Dlc1* did not affect the other two species produced from the same locus and did not produce alterations in the expression levels of transcripts in the same chromosomal region.

Since the deletion of intron 1 in the circ-KO mice produced a strong decrease of the full-length *lin-Dlc1* transcript, we raised an additional mouse strain (lin-KO) where the expression of this specific isoform is prevented through the insertion in the exon 4 of a premature polyadenylation site (PAS) coupled with two MAZ transcriptional pausing sites (Figure S2D). This mutant represents an important control in order to exclude any contribution of the full-length linear transcript toward the potentially emerging phenotype. PCR on genomic DNA from mouse tail snips revealed the proper insertion of the desired sequences (Figures S2E and S2F). Real-time qPCR on total RNA extracted from the striatum of adult wild-type (WT) and lin-KO mice showed that the expression of *lin-Dlc1* was impaired beyond exon 4 by the premature PAS, while the levels of *circDlc1(2)*, *Dlc1-201*, and *Dlc1-203* transcripts were unaffected (Figure S2G).

circ-KO mice have an upregulated glutamatergic response pathway in the striatum

The striatum was chosen for proteomics analysis as opposed to the prefrontal cortex because its dissection is more "consistent." Unlike the striatum, which is collected whole, the prefrontal cortex should be separated from the remainder of the cortex via resection; moreover, in this district, *circDlc1(2)* appeared differentially expressed in the different layers, meaning that the sample itself may be less uniform in terms of composition. In addition, the striatum is a good candidate, as this brain region processes information received from the cortex.

We then compared mass spectrometry (MS)-based proteomics analysis of the striatum of circ-KO and syngeneic WT animals. Interesting differences were observed, and among the deregulated proteins (Table S1), there was the significant variation of three genes, *Grin2a*, *Grin2b*, and *Camk2a*, commonly found in specific Gene Ontology (GO) classes corresponding to long-term potentiation (LTP), NMDA-related circuitries, and post-synaptic events (Figures 2A and 2B). In addition, *Gria1*, which encodes for a subunit of the AMPA receptor, resulted as one of the most upregulated genes (Table S1; Figure 2B).

The above-mentioned genes were tested for their expression level in striatal tissues, and *Grin2a*, *Grin2b*, and *Camk2a* mRNAs were found to be significantly increased, while *Gria1* remained at control levels (Figure 2C). These transcripts, here named

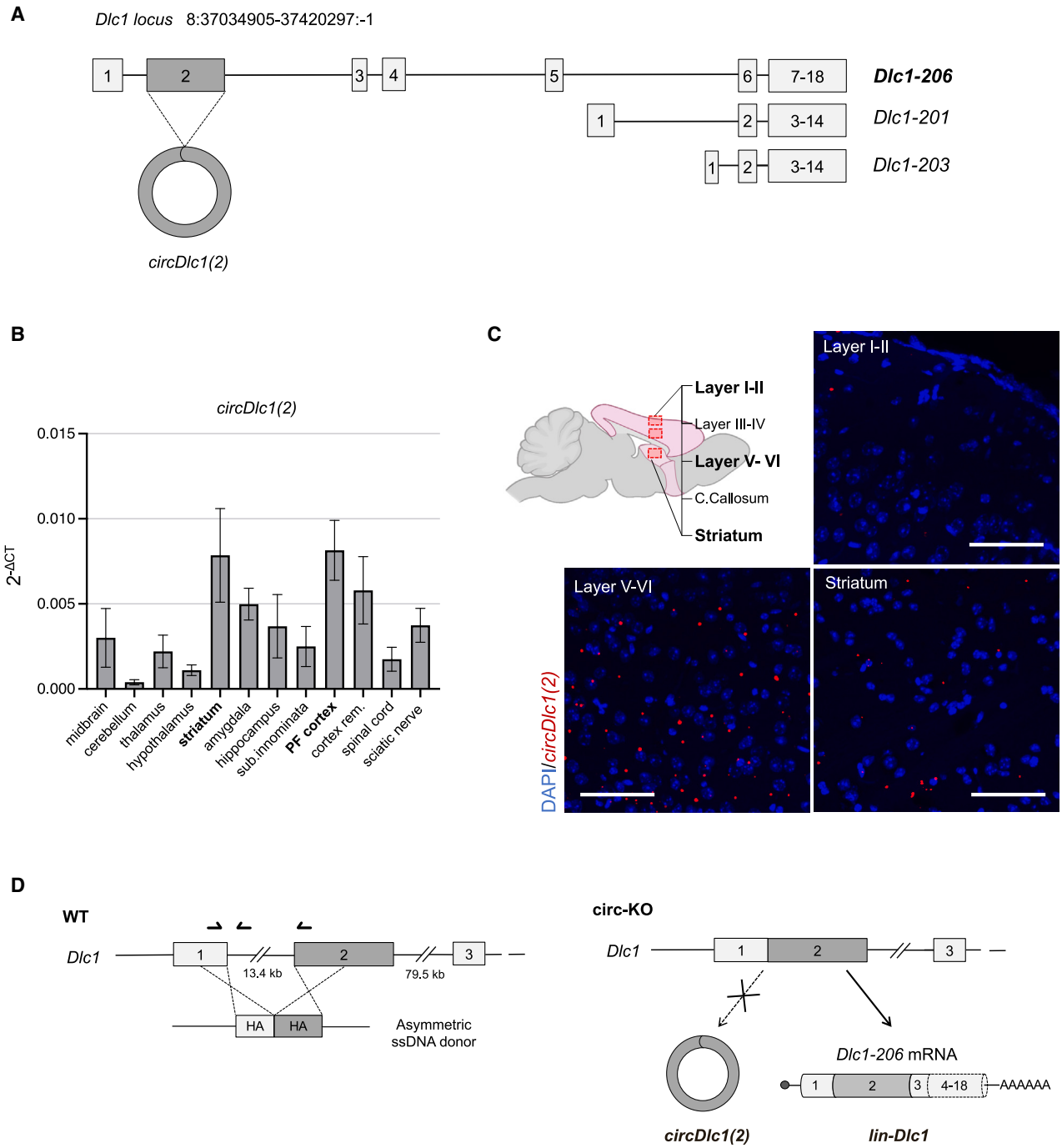

Figure 1. *circDlc1(2)* locus and expression analysis

(A) Schematic representation of the *Dlc1* mouse genomic locus including the three linear isoforms and the circular isoform of interest.

(B) Relative expression of *circDlc1(2)* in several brain districts, expressed as relative enrichment with respect to *Ybx1* standard gene. Error bars represent the ΔCT SEM (n = 3).

(C) Detail enlargement from Figure S1 for cortex layers I-II, V-VI, and the striatum. Scale bar, 150 μm

(D) CRISPR-Cas9 strategy employed to generate homozygous circ-KO (right) animals. Primers used for the genotyping (see Figure S2A) are mapped on the WT locus (left).

See also Figures S1 and S2.

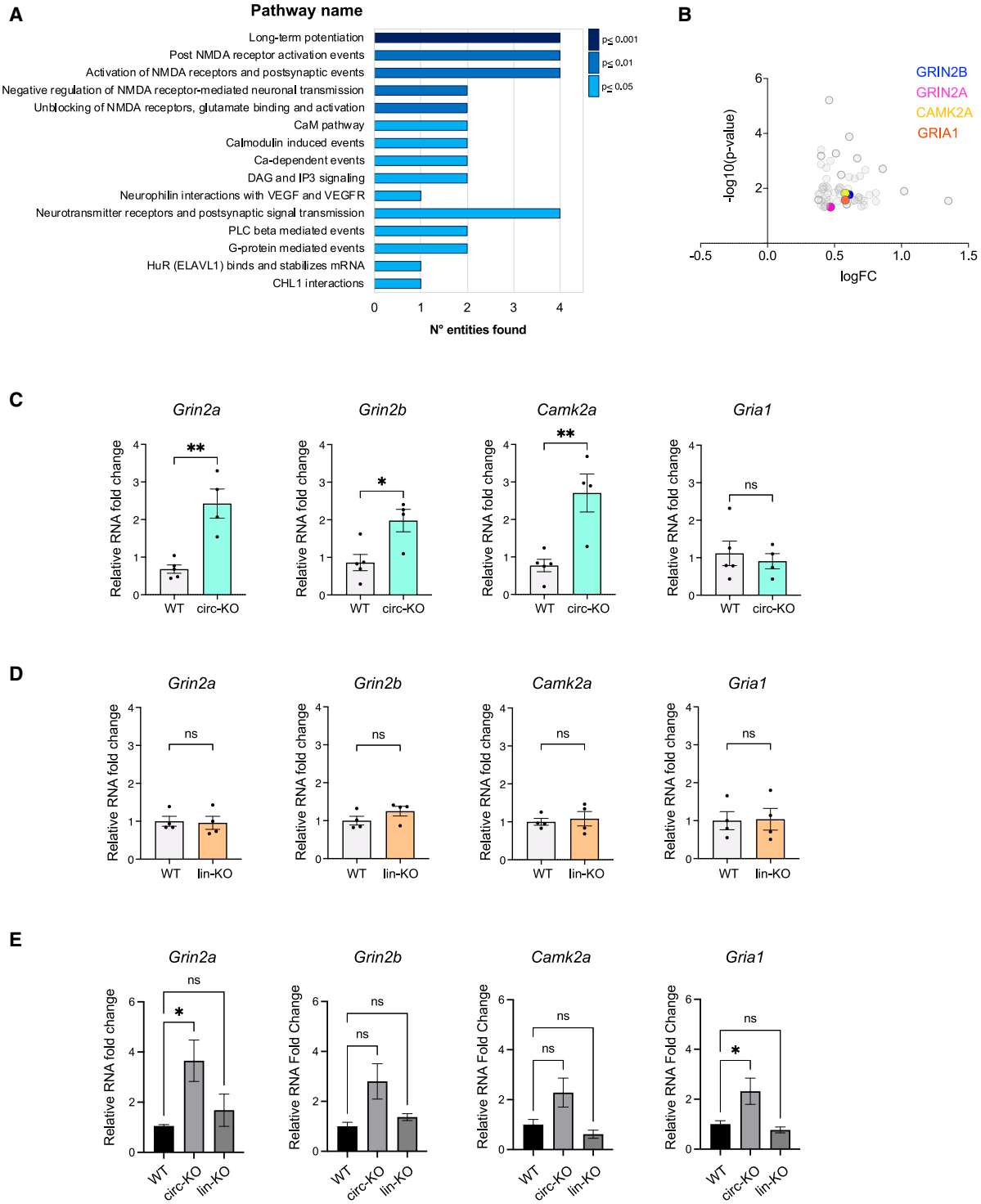

Figure 2. Proteomics and real-time qPCR analyses of genes deregulated in the striatum of circ-KO mice

(A) Functional enrichment analysis of the differentially expressed genes derived from mass spectrometry analysis of WT and circ-KO striatum-derived extracts (n = 6 per genotype) performed using the Reactome pathway database.

(B) Volcano plot showing the differentially expressed proteins between WT and circ-KO. Genes of interest (*gluRNAs*) are shown with colored dots.

(legend continued on next page)

gluRNA, were selected for further studies. The analysis of their primary transcripts did not reveal any increase (Figure S3A), indicating that the effect of *circDlc1(2)* KO was exerted at the post-transcriptional level, including stability and translational control. Notably, the levels of *gluRNA* did not change in the lin-KO animals, indicating the specificity of activity of the circular isoform on this set of transcripts (Figure 2D).

To further validate the impact of *circDlc1(2)* on the identified glutamatergic alterations, we raised mouse embryonic stem cells (mESCs) from WT and syngeneic circ-KO animals and differentiated them *in vitro* following a physiological dopaminergic differentiation, which leads to a mixed population including GABAergic and glutamatergic neurons as previously shown by Lee et al.[27] (Figure S3B). The presence of the different cellular subtypes was validated by checking the relative expression of specific markers: neuronal progenitors (identified by *Nestin* expression) appeared at day 12, while markers for glutamatergic and GABAergic (*Ctip2*), dopaminergic (*Foxa2* and *Th*), and medium spiny (*Darpp32*) neurons appeared at day 17 (Figure S3C). Interestingly, no difference in the expression of markers specific for the different cell types was found between circ-KO and WT cells, indicating that the cell type composition is similar in the two systems (Figure S3D). Furthermore, *circDlc1(2)* expression peaked during a window of time from day 12 to 17 but was still expressed at day 30 (Figure S3C). In this *in vitro* cellular system, we observed similar *gluRNA* upregulation to that in circ-KO animals; in particular, *Gria1* and *Grin2a* showed a significant upregulation, while *Grin2b* and Camk2a, though not significant, showed a similar trend (Figure 2E). Notably, the same analysis performed in lin-KO cells did not show any variation of the same *gluRNA* (Figure 2E). Altogether, these data indicated a clear upregulation of *gluRNA* only in circ-KO conditions.

Increased AMPA-mediated response in circ-KO-derived neurons

In light of the upregulation of glutamatergic-related circuitries, we decided to perform time lapse calcium imaging recordings on mESC-derived neurons. Previous work indicated that, through the differentiation protocol used (Figures S3B and S3C), neurons are physiologically active around day 30.[27] In order to assess the suitability of these cells for calcium imaging analyses, we validated the upregulation of glutamatergic response-associated genes at this time point (Figure S4A), together with that of the circRNA, and checked the formation of glutamatergic synapses revealed by the presence of overlapping immunofluorescence (IF) signals for GRIA1 and VGLUT2 (Figure S4B). We then evaluated the efficacy of the AMPA agonist to mediate a specific response in control, circ-KO, and lin-KO neuronal cultures. We measured calcium transients evoked by a local and brief application of AMPA applied on neuronal culture through a puffer pipette together with cyclothiazide (CTZ) to reduce receptor desensitization and allow more precise quantification of the calcium signals[28,29] (Figure 3A). AMPA+CTZ application evoked a fast-rising calcium transient indicating the presence of functional glutamatergic receptors in all cultures, where AMPA-mediated calcium transient was significantly higher in circ-KO neurons with respect to both control and lin-KO neurons (Figure 3B). Specifically, the mean peak amplitude of the calcium response was 11% higher in circ-KO neurons compared to WT and 23% higher with respect to lin-KO (Figure 3C), thus confirming a higher expression of AMPA receptors specifically on the circ-KO neuronal surface.

Loss of *circDlc1(2)* function leads to hyperactivity, stereotyped behaviors, and behavioral disinhibition

In order to correlate the biochemical and calcium imaging data with possible functional defects, we performed several behavioral tests. circ-KO mice showed no neuromuscular impairment when tested with hanging steel and hanging wire, which are muscular endurance tasks (Figures S5A–S5C). Since the fronto-striatal system regulates goal-directed exploratory behaviors in novel environments,[30] we evaluated them in the open field tests. circ-KO mice showed an increase in spontaneous locomotor activity (Figure 4A) and mean speed (Figure 4B) compared to WT, suggesting that they are hyperactive; moreover, circ-KO mice also spent more time in the center of the open field (Figure 4C), which is generally associated with reduced anxiety in mice,[31] thus further indicating behavioral disinhibition.

The scoring of stereotypies (repetitive movement sequences) during the open field test highlighted that mutant mice show a non-statistically significant reduction of self-grooming behavior (Figure 4D) and a significant increase in rearing (Figure 4E), a compulsive behavior in which mice repetitively stand on their hind legs, compared to WT littermates. No specific alteration in associative memory was detected in the contextual fear conditioning task, in which mice learn, during the training phase, to associate a context with a mild foot shock. 24 h later, their memory is tested by exposing them to the context in the absence of the foot shock; freezing time is considered to be an index of long-term associative memory. circ-KO mice showed the same freezing response as WT mice (Figure 4F).

The same tests were performed on lin-KO mice, which did not show any variation with respect to the WT littermates (Figures S5D–S5F and S6A–S6F), indicating a circRNA-specific contribution toward the analyzed phenotypes. Altogether, these data are consistent with hyperactivity of the cortico-striatal

(C) Real-time qPCR expression levels for glutamatergic mRNA targets of interest in WT and circ-KO mice ($n = 5$ and $n = 4$ respectively). Error bars represent the ΔCT SEM; RNA fold change ($2^{-\Delta\Delta CT}$) is relative to the average expression in WT animals (=1); *Hprt* was used as the calibrator; two-tailed, unpaired Student's t test where ns is not significant ($p > 0.05$), $^{*}p \leq 0.05$, and $^{**}p \leq 0.01$.
(D) As in (C) but for WT and lin-KO animals ($n = 4$ per genotype).
(E) Real-time qPCR expression levels for *gluRNA* targets of interest in WT, circ-KO, and lin-KO ($n = 3$ per genotype) mESC-derived neurons at day 30 of differentiation. Error bars represent the ΔCT SEM; RNA fold change ($2^{-\Delta\Delta CT}$) is relative to the average expression in WT cells (=1); *Atp5o* was used as the calibrator; one-way ANOVA where ns is not significant ($p > 0.05$) and $^{*}p \leq 0.05$.
See also Figure S3 and Table S1.

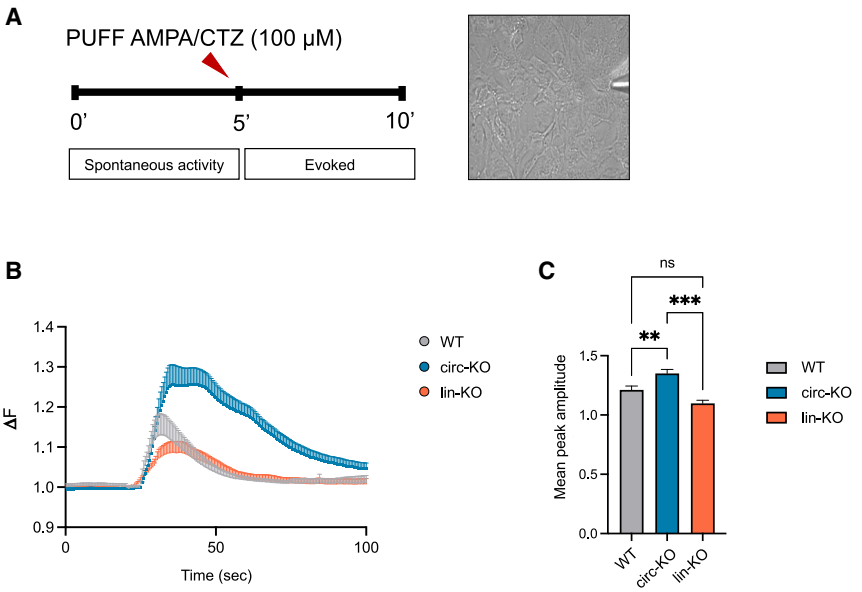

Figure 3. AMPA-mediated response in WT, circ-KO, and lin-KO neurons

(A) Schematic representation of the time course of AMPA/CTZ application (left) on neuronal culture through a puffer pipette (right).

(B) Mean calcium transient response of WT (gray), circ-KO (blue), and lin-KO (orange) neurons in response to puff application of 100 μM AMPA and CTZ (WT n = 81/10/3 cells/FOVs/batches, circ-KO n = 96/12/3 cells/FOVs/batches; lin-KO n = 29/9/3 cells/FOVs/batches). ΔF represents the difference in fluorescence between spontaneous and evoked activity.

(C) Bar chart representing the mean peak amplitude value for WT, circ-KO, and lin-KO cells (one-way ANOVA where ns is not significant ($p > 0.05$), $^{**}p \leq 0.01$, and $^{***}p \leq 0.001$). Error bars represent the SEM.

See also Figure S4.

pathway resulting in increased behavioral disinhibition and increased stereotypies[32] due to the specific lack of *circDlc1(2)*.

circDlc1(2) binds miR-130b-5p and *gluRNA*

In consideration of the *in vitro* and *in vivo* relevance of the identified glutamatergic alterations, we deepened our analysis by trying to correlate the functional link between *circDlc1(2)* and *gluRNA*. In line with the knowledge that circRNAs often work through miRNA binding, we carried out computational analyses in order to predict the miRNAs capable of interacting with both *circDlc1(2)* and the 3′ UTRs of mRNAs that code for proteins altered in the above-mentioned MS-based analysis (Figure 5A). miRNAs expressed in the murine striatum were retrieved by accessing two different datasets (Dell'Orco et al.[33] and Eipper-Mains et al.[34]), and *in silico* predictions were performed using the miRanda tool.[35] The initial predictions identified miRNAs with putative sites on *circDlc1(2)*, which were also predicted to bind the 3′ UTRs of deregulated genes from the proteomics results. Only miRNAs with more than a single predicted site on *circDlc1(2)* were considered (Figures 5A and 5B). In particular, miR-130b-5p, miR-93-3p, miR-361-3p, and miR-345-5p appeared to be able to target the 3′ UTRs of the 4 *gluRNA*s (Figures 5B, S7A, and S7B). Notably, by employing an additional software, TargetScan,[36] we confirmed that miR-130b-5p was the only miRNA predicted to target all 4 *gluRNA*s (Figure S7C). We then tested the association of *circDlc1(2)* with the RNA-induced silencing complex (RISC) by performing a UV-cross-linked RNA immunoprecipitation (UV-CLIP) experiment with AGO2 antibodies in mESC-derived neurons. *circDlc1(2)* was enriched in the IP sample with respect to the immunoglobulin (Ig)G, similarly to control circRNAs known to have an elevated number of miRNA binding sites[37,38] (Figure 5C).

To experimentally prove the interaction of these miRNAs, we performed a pull-down (PD) of *circDlc1(2)* using murine striatal tissue. We selected six probes, including one overlapping the back-splicing junction (BSJ), that did not overlap with the putative miRNA binding sites in order to avoid competition for miRNA binding. Figure 5D (left) shows that *circDlc1(2)* was retrieved by the specific probes (PD *circDlc1(2)*), while it was undetectable when using negative control probes (PD *lacZ*). The analysis of the miRNAs recovered in the PD fraction indicated a specific enrichment for miR-130b-5p but not for miR-93-3p, miR-361-3p, and miR-345-5p (Figure 5D, right). miR-493-5p was chosen as a negative control, as it was not predicted to interact with the circRNA and its expression levels are similar to those of miR-130b-5p.[33] Since the probes were designed on the exon 2 portion, partial enrichment of the linear *Dlc1* counterpart was observed, while no enrichment was detected for the negative control *Atp5o* (Figure 5D, left). An additional PD experiment was performed with a BSJ-specific probe in order to prevent the co-PD of the linear counterpart. The results indicate that the PD was restricted to *circDlc1(2)* without any contamination of the linear isoform (Figure S8A, left); also, in this case, miR-130b-5p was found to be specifically enriched in the PD fraction (Figure S8A, right), confirming its association to the circular form.

As previous work has shown that circRNA-miRNA interactions can be important for the stability of the miRNA,[35] we checked the expression levels of miR-130b-5p in the striatum of WT and circ-KO animals. Notably, the depletion of *circDlc1(2)* resulted in no specific effect on the miRNA levels (Figure S8B). Similarly, miR-130b-5p levels were unchanged in circ-KO and WT in mESC-derived differentiated neurons at day 30 (Figure S8C).

The ability of *circDlc1(2)* to bind miR-130b-5p, together with the finding that the predicted miR-130b-5p targets are up-regulated in circ-KO conditions, excluded the possibility of *circDlc1(2)* acting as a miR-130b-5p sponge and suggested an alternative function. Therefore, we searched for other possible mechanisms explaining the upregulation of *gluRNA*. A computational prediction revealed that *circDlc1(2)* has a higher thermodynamic affinity for *gluRNA*s compared to their controls with similar properties (overall length and similar size of the 5′ UTRs, coding sequences, and 3′ UTRs). This is not the case for all other mRNAs encoding proteins upregulated in the circ-KO (Figures 5E and S8D; Table S4). We therefore performed

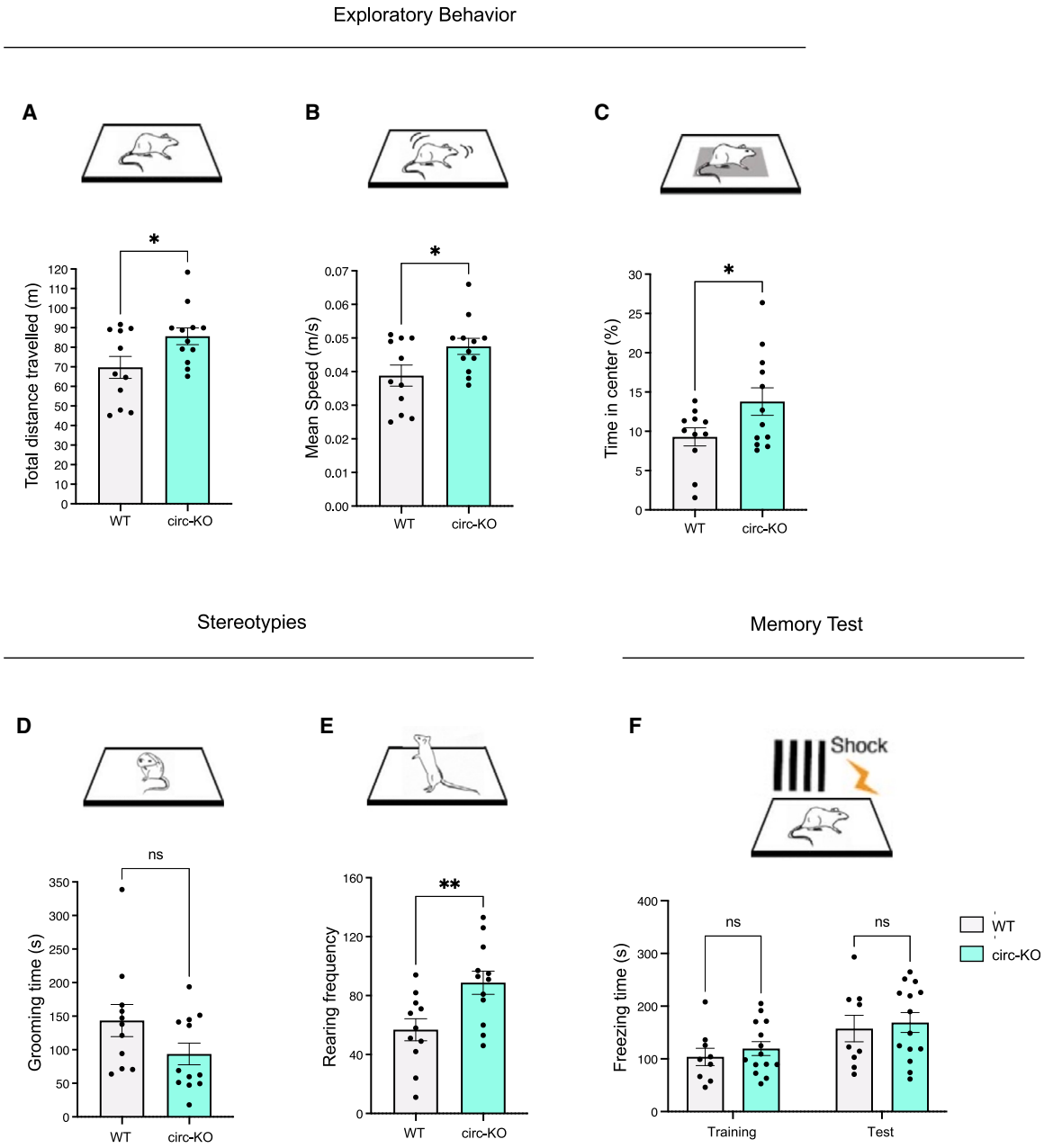

Figure 4. Functional tests performed on 6-month-old WT and circ-KO mice

(A–C) Exploratory behavior evaluated in the open field test (WT $n = 11$; circ-KO $n = 12$) via the following parameters: (A) total distance traveled, (B) average speed, and (C) percentage of time spent in the center of the arena.

(D and E) Assessment of stereotypical behavior through (D) time spent self-grooming and (E) the frequency of rearing (WT $n = 11$; circ-KO $n = 12$).

(F) Fear conditioning test to assess associative memory (WT $n = 9$; circ-KO $n = 14$). Error bars represent the SEM. Statistical analysis was performed with unpaired two-tailed t tests, where ns is not significant ($p > 0.05$), $^{*}p \leq 0.05$, and $^{**}p \leq 0.01$.

See also Figures S5 and S6.

circDlc1(2) PD experiments using striatal tissue with a collection of probes covering different regions of the circRNA but excluding the best putative *gluRNA* pairing regions (Figure S8E). Indeed, this approach enabled the validation of the predicted interactions for *Grin2a* and *Gria1 gluRNA*s (Figure 5F), while two mRNAs predicted not to interact with *circDlc1(2)* were enriched in the PD fraction at levels similar to the negative controls. A different scenario emerges for *Camk2a*, which is enriched in the PD fraction to a much lesser extent compared to *Grin2a* and *Gria1* but still at a higher level than the negative controls. (Figure 5F). Since a contamination of the linear isoform was observed in the retrieved fraction, we performed, as control, a PD assay using antisense

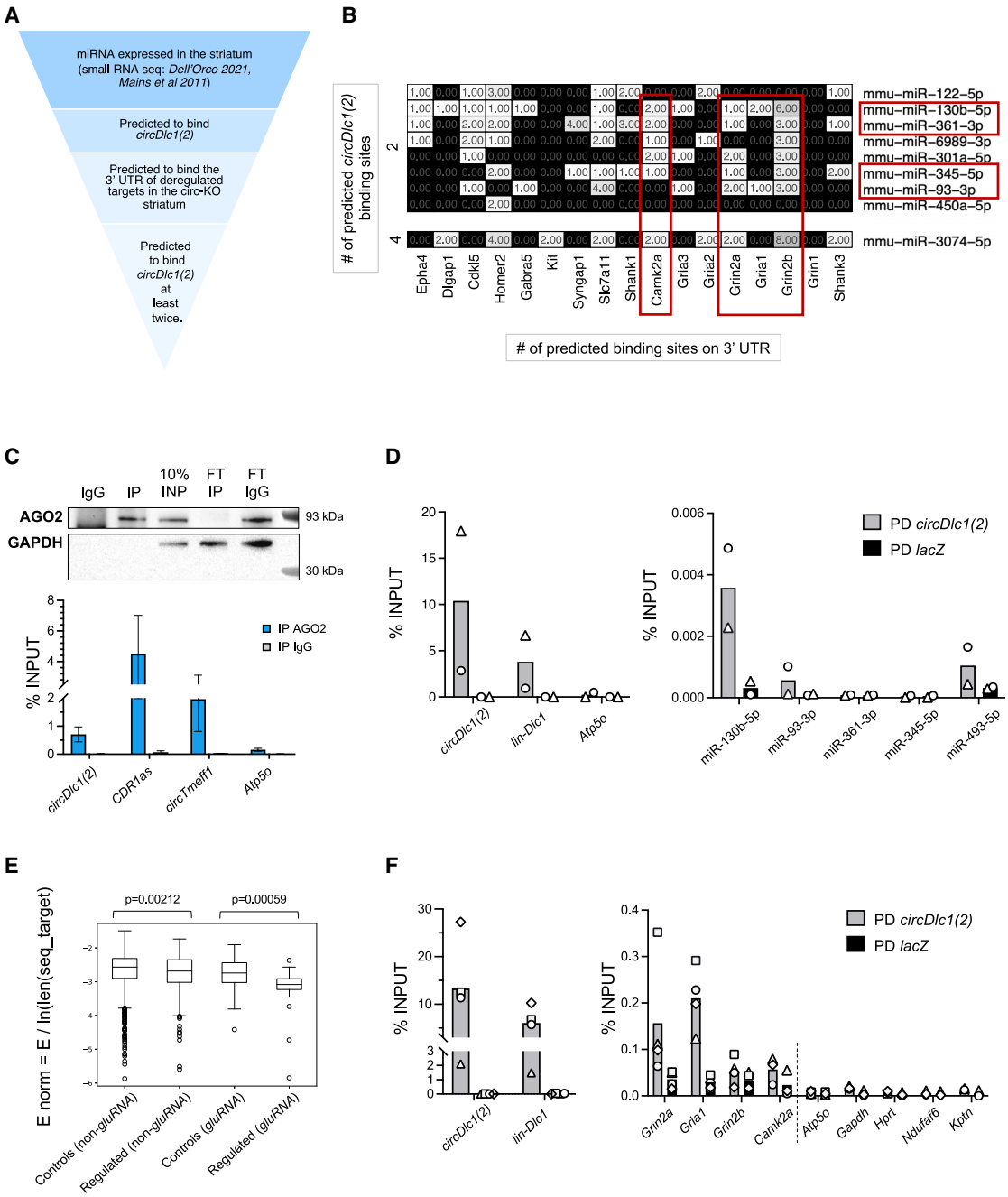

Figure 5. *circDlc1(2)* RNA interaction partners

(A) Computational workflow of the *in silico* miRNA-RNA target interaction predictions represented in (B).

(B) Heatmap enlargement derived from Figure S7A. Genes and miRNAs of interest are boxed in red. Each cell corresponds to the number of predicted binding sites for the miRNAs on the target mRNA 3′ UTRs based on the Dell'Orco et al.[33] dataset.

(C) RNA crosslinked immunoprecipitation assay for AGO2 performed in neuronal precursor cells. Top: representative image of the immunoblot for AGO2 of the retrieved protein fraction with GAPDH used as a negative control. FT is the flowthrough for both IP and IgG fractions. Bottom: real-time qPCR quantification of *circDlc1(2)* enrichment in the IP and IgG samples relative to the input. *CDR1as* and *circTmeff1* were used as positive controls,[37,38] while *Atp5o* was used as a negative control (n = 3). Error bars represent the SEM.

(D) Native RNA PD assay performed on total striatum extracts. Left: real-time qPCR quantification of *circDlc1(2)*, *lin-Dlc1*, and negative control *Atp5o* enrichment in PD-*circDlc1(2)* and PD-*lacZ* samples relative to the input. Right: real-time qPCR quantification of miRNAs of interest shown in (B) in the same PD-*circDlc1(2)* and *lacZ* samples with miR-493-5p as the negative control. Individual values are expressed as input percentages and displayed as different symbols.

(E) Boxplot depicting the interaction energy (normalized on target length) of *circDlc1(2)* with non-*gluRNA* and *gluRNA*, each compared to their respective control group. Statistical significance was assessed using a two-tailed Mann-Whitney U test, and exact p values are shown.

(legend continued on next page)

oligonucleotides specific only for the linear transcript. The results show that none of the *gluRNA*s tested were retrieved through this PD, thus indicating that only the circular form holds the ability to interact with *gluRNA* (Figure S9A). Due to the strong enrichment of *Gria1* and *Grin2a*, we selected these mRNAs for further investigation. In both cases, the putative pairing regions with *circDlc1(2)* are located in their 3′ UTRs (Figure S8F).

miR-130b-5p and *circDlc1(2)* are both required for the control of *gluRNA* expression

To delve more deeply into the mechanism of the *circDlc1(2)*/miR-130b-5p/*gluRNA* interplay, we made use of luciferase reporter constructs and started by testing their responsiveness to miR-130b-5p action. The mouse neuronal Neuro-2a (N2a) cell line was selected since it can be efficiently transfected and expresses both *circDlc1(2)*[19] and miR-130b-5p (Figure S9A). The *circDlc1(2)* sequence containing miR-130b-5p responsive elements (130-MREs; Figure S9B), when inserted downstream of the luciferase reporter gene (*circ-WT*), reduced the luciferase levels in the presence of miR-130b-5p mimics (Figure 6A). No significant reduction of luciferase activity was instead observed when testing the construct lacking the two 130-MREs with the best predicted interaction energy (*circ*-mut) (Figures 6A and S9B). The greater variability in luciferase activity produced by using this latter construct may be due to the additional miR-130b-5p target sites identified by using the combination of miRanda (including suboptimal thresholds) and Targetscan (Figure S9B and S9C). A reduction of luciferase activity was also observed when the portion of the *Gria1* 3′ UTR containing two 130-MREs (*Gria1-WT-S*) was tested in the presence of miR-130b-5p mimics (Figure 6B). A similar effect was observed when analyzing the 3′ UTR of *Grin2a* carrying one 130-MRE (*Grin2a-WT*; Figure S10A). On the contrary, no variation in the luciferase activity was observed when both mutant derivatives lacking the 130-MREs (*Gria1-mut-S* and *Grin2a-mut*) were tested in the presence of miR-130b-5p mimics (Figures 6B and S10B, respectively), indicating that indeed, these 3′ UTRs are responsive to the repression exerted by miR-130b-5p.

Next, we investigated the contribution of the *circDlc1(2)*/*gluRNA* pairing on miRNA repression in the presence or absence of *circDlc1(2)*. We performed *circDlc1(2)* knockdown (KD) experiments with short interfering RNAs (siRNAs) against the BSJ, obtaining a downregulation of ∼90% for *circDlc1(2)* but not for *lin-Dlc1* (Figure S10C, left). In such conditions, the levels of miR-130b-5p remained unaltered (Figure S10C, right). For such analyses, we compared three different constructs (diagrams in Figure 6C): *Gria1-WT-L*, containing the entire 3′ UTR including the 130-MRE and the *circDlc1(2)* pairing region; *Gria1-WT-S*, which lacks the *circDlc1(2)* pairing region; and *Gria1-ΔmiR*, lacking the 130-MRE. In comparison to the *Gria1-WT-S* construct, *Gria1-WT-L* produced a significant increase of luciferase activity when the endogenous *circDlc1(2)* was downregulated (Figure 6C, left). Notably, the *Gria1-ΔmiR* construct also produced higher luciferase levels in the absence of *circDlc1(2)* (Figure 6C, left). The same results were obtained with the *Grin2a-WT* construct upon downregulation of *circDlc1(2)*; namely, the luciferase activity was increased, as well as that of the mutant derivative lacking the 130-MRE (Figures S10A and S10B).

These data suggest that *circDlc1(2)* may also regulate *Gria1* and *Grin2a* independently from the presence of MREs in the 3′ UTR, and altogether, these results corroborate what was observed *in vivo*, where the lack of *circDlc1(2)* increases the protein levels of the target *gluRNA*.

To further support these findings, the overexpression of *circDlc1(2)* (Figure S10D) provided the opposite effect by repressing the luciferase of the *Gria1-WT-L* and *Gria1-ΔmiR* constructs and not that of *Gria1-WT-S* (Figure 6C, right), which lacks the circRNA pairing region. In addition, the combined action of siRNAs against *circDlc1(2)* together with locked nucleic acids (LNA) against miR-130b-5p was synergistic in the upregulation of luciferase activity on the *Gria1-WT-L* construct (Figure 6D).

Then, we tested the *Gria1-WT-L* construct, containing the entire 3′ UTR and its 130-MRE mutant derivative (*Gria1-mut-L*), for its ability to respond to miR-130b-5p mimics and *circDlc1(2)* depletion. Figure 6E shows that only the luciferase activity from *Gria1-WT-L* decreases in the presence of miR-130b-5p mimics (left), while *circDlc1(2)* depletion causes a reduction of luciferase activity from both *Gria1-WT-L* and *Gria1-mut-L* constructs (right). These results confirm that miR-130b-5p and *circDlc1(2)* can directly control *Gria1* expression by binding two different regions in the 3′ UTR.

In order to exclude any contribution of the linear *Dlc1* isoform to these regulatory networks, we tested the luciferase activity of *Gria1-WT-S*, *Gria1-WT-L*, *Gria1-ΔmiR*, and *Grin2a-WT* in N2a cells treated with siRNAs against exon 5 of *lin-Dlc1* (Figure S11A), which specifically downregulates the *lin-Dlc1* isoform without any effect on the circular counterpart (Figure S11B, left). We also observed that miR-130b-5p levels did not vary (Figure S11B, right). In none of the cases did we observe significant variations of the luciferase activity (Figures S11C–S11F), further demonstrating the specific effect of the circular isoform.

Finally, since the stoichiometry between two interacting partners is important for the proper functioning of the regulatory circuitry, we performed absolute quantification of *circDlc1(2)*, *Gria1* mRNA, and miR-130b-5p in mESC-derived neurons. This quantification revealed that the circRNA is 2-fold higher than the mRNA (44 vs. 23 molecules/ng of total RNA), while the miRNA is more abundant (704 molecules/ng of total RNA). This is in line with a role for *circDlc1(2)* in controlling the expression of Gria1 mRNA acting in synergy with miR-130b-5p, while the higher levels of the miRNA are compatible with the large number of targets that miRNA normally have.

Altogether, these results indicate that miR-130b-5p is a repressor of *gluRNA* and that it acts in conjunction with *circDlc1(2)*. We also show that *circDlc1(2)* can control the expression of *Gria1* by itself, likely through the multiple AGO

(F) Native RNA PD assay performed on total striatum extracts. Left: real-time qPCR quantification of *circDlc1(2)* and *lin-Dlc1* enrichment in PD-*circDlc1(2)* and *lacZ* samples relative to the input. Right: real-time qPCR quantification of *gluRNA* targets of interest in the same PD-*circDlc1(2)* and *lacZ* samples with negative controls after the dashed line. Individual values are expressed as input percentages and displayed as different symbols.
See also Figures S7 and S8 and Table S4.

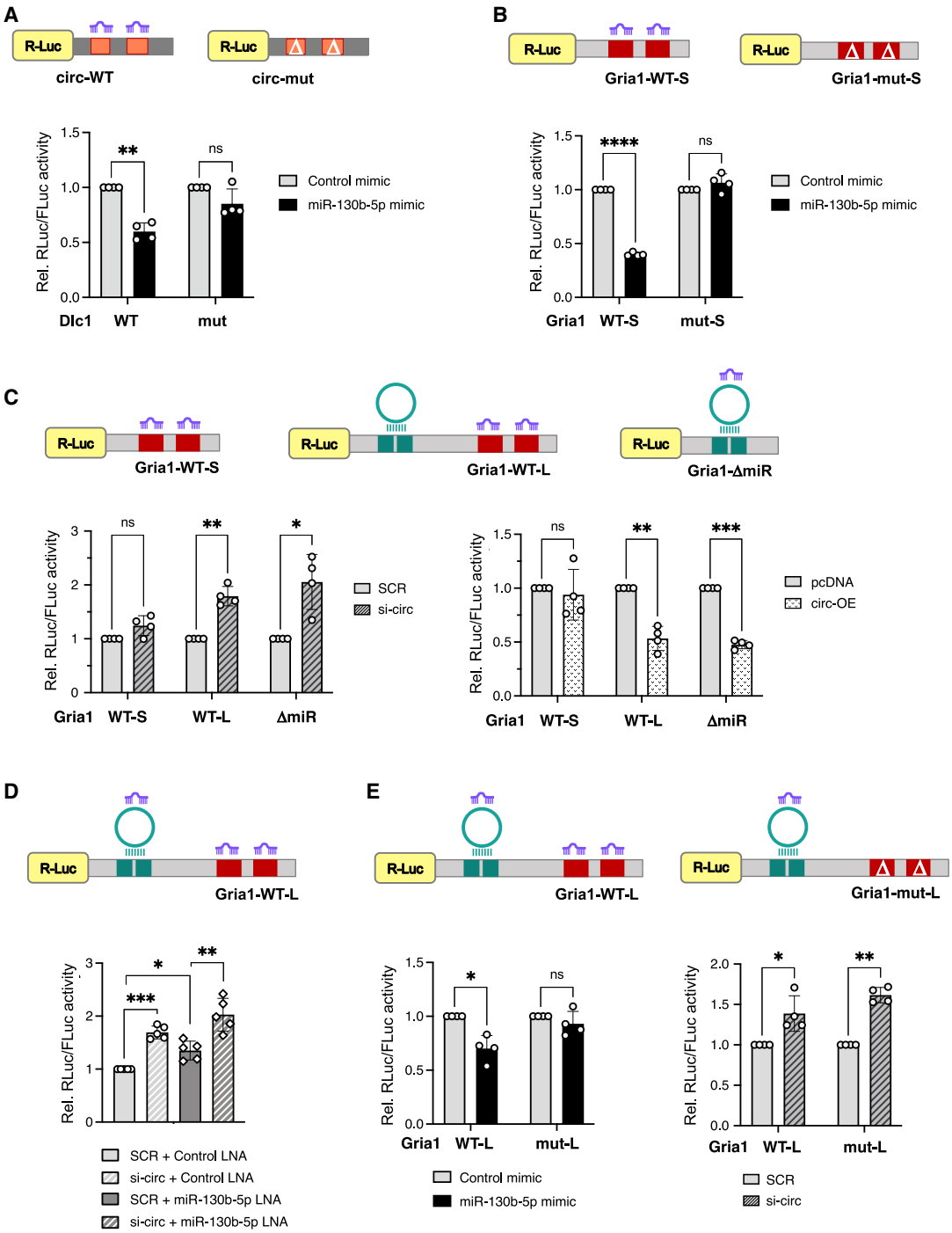

Figure 6. Regulation of *Gria1* expression, mediated by its interaction with *circDlc1(2)* and miR-130b-5p

(A) Relative luciferase activity in N2a cells co-transfected with the *Luc-circ-WT* or *mut* (mutant) construct and a control or miR-130b-5p mimic.

(B) Relative luciferase activity in N2a cells co-transfected with the *Luc-Gria1-WT-S* or *mut* construct and a control or miR-130b-5p mimic.

(C) Relative luciferase activity in N2a cells transected with *Luc-Gria1-WT-S*, *WT-L*, or *ΔmiR* constructs in si-*circDlc1(2)*/SCR (left) or *circDlc1(2)* overexpression (OE)/pc(plasmid coding)DNA conditions (right).

(D) Relative luciferase activity in N2a cells co-transfected with *Luc-Gria1-WT-L* and si-*circDlc1(2)*, LNA against miR-130b-5p, or both, with relative controls. White dots and diamonds represent control LNA and LNA against miR-130b-5p conditions, respectively.

(legend continued on next page)

proteins bound to it. However, we cannot exclude that it can also favor the tethering of the miRNA on the target mRNAs.

circDlc1(2) controls miR-130b-5p localization in neurites

Since *gluRNA*s have been described to be present at synaptic regions,[22,23] we wondered whether *circDlc1(2)* and miR-130b-5p are also localized in these compartments. FISH analyses, combined with IF for TUBB3, indicated that both RNAs are present in neurites (representative images in Figures S12A and S12B, left). We then tested the localization at synaptic regions by combining IF for the post-synaptic PSD-95 protein with FISH analyses. As shown in the representative images in Figure 7A, a noticeable fraction of both *circDlc1(2)* and miR-130b-5p co-localizes with PSD-95. This observation is corroborated by the evaluation of the Mander's overlap coefficient (MOC) quantification indicating the fraction of *circDlc1(2)* and miR-130b-5p signals overlapping with the PSD-95 protein (Figure 7B). As control, we used miR-132-3p, already known to be localized at synapses,[39] where it regulates the expression of its mRNA targets[40] (Figures 7A, 7B, and S12C, left). The *circDlc1(2)* signals localized with the PSD-95 protein with an MOC index that is comparable with that of miR-132-3p (∼0.2; Figure 7B), used as a positive control, indicating a clear co-localization that is not due to a random superimposition of signals.

Notably, miR-130b-5p showed a significantly higher spatial overlap with PSD-95 with respect to miR-132-3p (Figure 7B). The spatial association of *circDlc1(2)*, miR-130b-5p, and miR-132-3p with the post-synaptic marker PSD-95 was also confirmed by line-scan analysis (Figures S12A–S12C, right), which shows a clear overlap of the fluorescence intensity pattern along a line drawn in the image.

We then assessed whether *circDlc1(2)* plays a role in miR-130b-5p localization at the cell periphery. We therefore performed miRNA-FISH experiments combined with IF for TUBB3 in WT and circ-KO mESC-derived neurons. In circ-KO cells, we noticed a different localization of miR-130b-5p, which tends to be retained mostly in the soma with respect to the WT condition (Figures 7C and 7D, top). To investigate this aspect, we quantified the mean percentage of miR-130b-5p signals in neurites per cell. Through this procedure, we saw that in circ-KO neurons, miR-130b-5p showed a significant reduction in localization at neurites (Figures 7C and 7D, top). As a likely consequence of this reduction, the mutant condition had a tendency to form larger spots, with a resulting increase in the average area of the FISH signals (Figure 7D, bottom). Interestingly, the doxycycline (dox)-inducible ectopic overexpression of *circDlc1(2)* in circ-KO cells was able to rescue the presence of miR-130b-5p at synaptic regions and recover the WT spot size (circ-OE +dox; Figures 7C, 7D, and S13A).

As control, the lack of dox induction maintained values similar to the circ-KO conditions (circ-OE −dox; Figures 7C and 7D). Altogether, these data underline that *circDlc1(2)* and miR-130b-5p are localized at post-synaptic compartments and that the circRNA is responsible for the correct localization of the miRNA.

DISCUSSION

Although many data are currently available on the enrichment of circRNAs in the brain and their *in vitro* activities, very little is known about their *in vivo* relevance for brain function. To date, only a few examples of the brain-specific effect of circRNA depletion have been reported. *Cdr1as* KO animals display a mild phenotype of impaired sensorimotor gating, which is associated with neuropsychiatric disorders,[37] while *circHomer1a* KD affects behavioral flexibility.[41]

circDlc1(2) in vivo activity was studied by CRISPR-Cas9-mediated deletion of the intron of the *Dlc1* gene upstream of the exon undergoing circularization, with the resulting exon 1/exon 2 fusion preventing the back-splicing reaction and production of *circDlc1(2)*. Indeed, this intervention, while completely knocking out the circRNA isoform, partially affected the expression of the linear counterpart. Therefore, as control, we also raised a specific KO mouse for the linear *Dlc1* mRNA.

Notably, previous studies on the *Dlc1* locus focused only on the *Dlc1-201* short isoform and reported that homozygous embryos lacking the expression of this specific isoform died at early stages of embryogenesis.[24,25] Importantly, in our circ-KO mice, we did not observe any alteration of *Dlc1-201*, indicating that the phenotype we have observed is not correlated with the function of this linear isoform.

In vivo analysis of *circDlc1(2)* expression indicated the striatum and V and VI layers of the prefrontal cortex as the districts with the highest levels. In the striatum, we found that *circDlc1(2)* depletion correlated with the alteration of glutamatergic-associated circuits, including LTP, as we observed the upregulation of RNA and protein levels of specific post-synaptic-density-associated genes and NMDA-related circuits. Among them are *Grin2a* and *Grin2b*, which encode for different subunits of the NMDA-type glutamate receptors; *Gria1*, encoding a subunit of the AMPA receptor; and *Camk2a*, which instead acts downstream of the post-synaptic NMDA glutamate receptors to increase synaptic conductance. Interestingly, these alterations were not found in lin-KO mice depleted for the linear isoform, indicating that such effects were specifically due to circRNA depletion.

This glutamatergic pathway altered in the striatal district is correlated with the phenotypic alterations studied with open field behavioral tests. circ-KO animals had reduced anxiety and were hyperactive, indicating behavioral disinhibition. circ-KO animals also showed stereotypies as indicated by the significant increase in rearing. The striatum is a key hub in the basal ganglia for processing neural information from cortical glutamatergic inputs converging into striatal medium spiny

(E) Relative luciferase activity in N2a cells co-transfected with either *Luc-Gria1-WT-L* or *mut* constructs and (left) the miR-130b-5p mimic or (right) siRNAs against *circDlc1(2)*. Luciferase activity data are presented as the mean ± SEM shown with respect to controls set to a value of 1. Each replicate is represented by a white dot. Statistical analysis was performed with paired two-tailed t tests, where ns is not significant ($p > 0.05$), *$p \leq 0.05$, **$p \leq 0.01$, ***$p \leq 0.005$, and ****$p \leq 0.001$. See also Figures S9–S11.

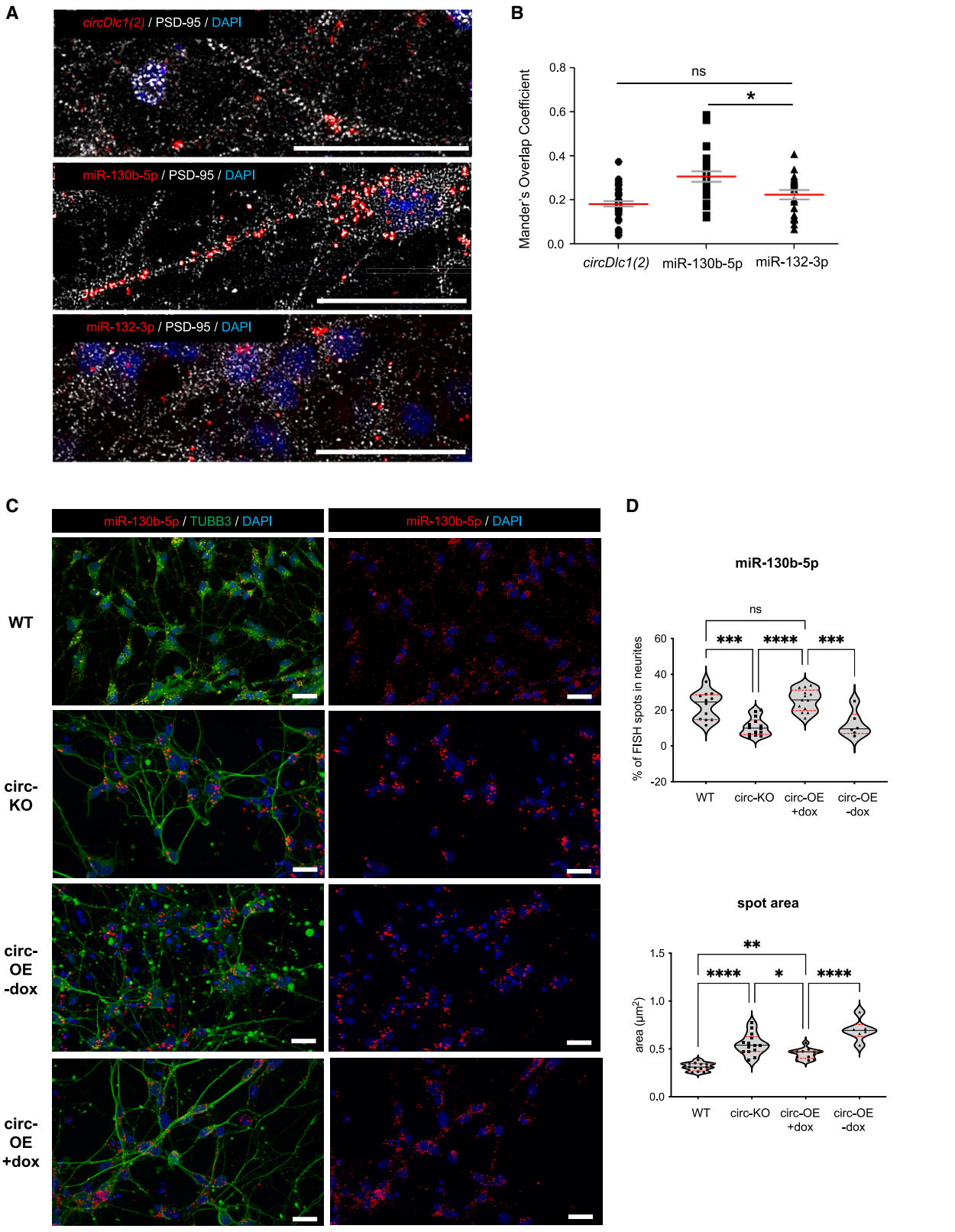

(legend on next page)

neurons. Indeed, the hyperactivation of this cortico-striatal pathway has been observed to have a positive effect on exploratory behavior by inducing hyperactivity and disinhibition.[42] Moreover, its increased activity can lead to stereotypies like rearing, meaning repeating stereotyped behavioral sequences over time. A recent study showed that exogenous activation of dorso-striatal neurons, which in turn engages the cortico-striatal-thalamo-cortical circuit, is sufficient for the onset of the same behavioral alterations observed in circ-KO mice.[43] Noticeably, the lack of impairment in associative contextual memory suggests an intact functionality of the Papez circuit,[44] which includes the hippocampus and amygdala, which is in line with lower *circDlc1(2)* expression in these areas as compared to the fronto-striatal region. An altered corticostriatal circuit is linked to various neuropsychiatric disorders, including attention-deficit hyperactivity disorder, Tourette syndrome, obsessive-compulsive disorder, autism spectrum disorder, and schizophrenia.[45,46]

The dissection of the molecular mechanism of action of *circDlc1(2)* resulted in the impingement of glutamatergic-specific signaling in a singular regulatory interplay with mRNAs and miRNAs. On one side, *circDlc1(2)* binds to several mRNAs deregulated in the circ-KO animals, the *gluRNA*s, and on the other, it physically interacts with their regulator, miR-130b-5p, and controls its localization at the neuron periphery. For two of these interactors, *Gria1* and *Grin2a*, we validated the ability of *circDlc1(2)* to act in a synergistic manner with miR-130b-5p in repressing translation, indicating that the circRNA does not act as a classical miRNA sponge but instead cooperates with the repressive activity of the miRNA.

The possibility that this effect could be due to miRNA destabilization by the circRNA has to be excluded since, in the absence of *circDlc1(2)*, the levels of miR-130b-5p were unaffected.

Even if a complete understanding of the *in vivo* effects of the perturbation of this circuitry will require further investigation, our data suggest an unprecedented model of circRNA function by which *circDlc1(2)* may act as a platform by tethering together miR-130b-5p and its gluRNA targets. This creates functional ribonucleoprotein (RNP) complexes where the AGO proteins, bound to both the circRNA and miRNA, can act synergistically on the target mRNAs. This is different from the mechanism of a canonical ceRNA (competing endogenous RNA) where the circRNA acts by sequestering miRNA molecules, removing their inhibitory activity on the mRNA targets.

Furthermore, the ability of *circDlc1(2)* to ensure efficient compartmentalization of miR-130b-5p to neuronal projections leads to a general model in which *circDlc1(2)* not only aids the physical proximity between miR-130b-5p and its mRNA targets but guarantees miRNA localization at synaptic regions, where *gluRNA*s have been shown to localize and their translation is controlled.[22,23]

These features are intriguing when considering the type of regulation required at peripheral neuronal districts, where localized translation should be finely regulated in response to specific stimuli; such a "ménage à trois" of three different types of RNAs adds another layer of circRNA-mediated regulation in neurons where compartmentalization ensures a robust control of gene expression.

Limitations of the study

Although this study offers new insights into the regulatory roles of circRNAs, it is limited by an incomplete understanding of the perturbation of the circRNA/miRNA/gluRNA network *in vivo*. Addressing this limitation will necessitate further research.

RESOURCE AVAILABILITY

Lead contact

Further information and requests for resources and reagents should be directed to and will be fulfilled by the lead contact, Irene Bozzoni (irene.bozzoni@uniroma1.it).

Materials availability

All materials generated in this study will be available upon request from the lead contact under a material transfer agreement.

Data and code availability

- All the proteomics data related to this work have been uploaded in the PRIDE database under the identifier PXD054407. Instructions for access can be found in Table S1.
- This paper does not report original code.
- Any additional information required to reanalyze the data reported in this paper is available from the lead contact upon request.

ACKNOWLEDGMENTS

We would like to thank N. Humphreys and M. Ascolani from the Gene Editing and Embryology Facility (GEEF) at EMBL-Rome for their help with the generation of the mutant mouse lines and A. Pisaniello for deriving mESC clones. We

Figure 7. *circDlc1(2)* and miR-130b-5p localization *in vitro*

(A) Representative RNA-FISH for *circDlc1(2)* (red; top), miR-130b-5p (red; middle), miR-132-3p (red; bottom), IF for PSD-95 (gray), and DAPI (blue) in WT cells at day 26 (top) or day 15 (middle and bottom) of differentiation. The image on top is a digital enlargement of Figure S12A, the middle is a digital enlargement of Figure S12B, the bottom is a digital enlargement of Figure S12C.

(B) Histogram showing the distribution of the Mander's overlap coefficient (MOC) in WT cells. The values indicate the ratios of the *circDlc1(2)*/PSD-95, miR-130b-5p/PSD-95, and miR-132-3p/PSD-95 overlaps, derived from the analysis of #1025, #531, and #419 cells respectively ($n = 3$). Mean MOC values and error bars ±SEM are indicated as red and gray lines, respectively.

(C) Representative images of RNA-FISH for miR-130b-5p (red) combined with IF for TUBB3 (green) and DAPI (blue) in WT, circ-KO, and circ-OE −/+dox cells at day 15 of differentiation.

(D) Top: violin plot indicating the percentage of miR-130b-5p signals located in neurites with respect to the total FISH signals (soma+neurite). Bottom: violin plot showing the mean area of the FISH spots. Each quantification is derived from the analysis of #1224, # 338, #177, and #514 cells, respectively ($n = 3$). Median and quartiles are indicated as a solid black line and dashed red lines, respectively. One-way ANOVA was performed, where ns is not significant ($p > 0.05$), $^{**}p \leq 0.01$, $^{***}p \leq 0.005$, and $^{****}p \leq 0.001$. All scale bars represent to 20 μm.

See also Figures S12 and S13.

also thank Marcella Marchioni for technical help and Manuela Caruso for assistance. This work was partially supported by the following grants: ERC-2019-SyG 855923-ASTRA, AIRC IG 2019 Id. 23053, "National Center for Gene Therapy and Drug based on RNA Technology" (CN00000041), and NextGenerationEU PNRR MUR to I.B.; Fondi di Ateneo Ricerca di base Università di Perugia to M.M.; PRIN-PNRR 2022 2022CFP7RF, Regione Lazio FSE 2014–2020 (19036AP000000019 and A0112E0073), and NextGenerationEU PNRR MUR B83C22002820006 to S.D.A.; and PRIN 2017 and BIOMARKERS MUR to E.D.L. B.M. was supported by PNRR-MAD-2022-12375960 Next Generation EU-PNRR M6C2 Investimento 2.1 valorizzazione e potenziamento della ricerca biomedica del SSN. This work is dedicated to the memory of Prof. Francesco Amaldi, who founded the lab and whose scientific and teaching legacies will forever remain a great example.

AUTHOR CONTRIBUTIONS

Conceptualization, I.B. and M.M.; methodology, V.S. and E.D.; validation, V.S., E.D., T.S., S.D., N.S., C.N., B.M., and D.C.; formal analysis, A.S. and N.L.; investigation, V.S., E.D., T.S., S.D., N.S., C.N., R.S., B.M., and D.C.; resources, F.C., C.N., L.F., E.D.L., D.R., and A.A.; data curation, A.S. and N.L.; writing – original draft, V.S. and E.D.; writing – review & editing, I.B. and M.M.; supervision, E.D.L., D.R., and A.A.; project administration, I.B. and M.M.; funding acquisition, S.D.A., E.D.L., I.B., and M.M.

DECLARATION OF INTERESTS

The authors declare no competing interests.

STAR★METHODS

Detailed methods are provided in the online version of this paper and include the following:

- KEY RESOURCES TABLE
- EXPERIMENTAL MODEL AND SUBJECT DETAILS
  - Generation of mouse lines
  - Cell culture conditions and treatments
- METHOD DETAILS
  - Mouse tissue collection for molecular analyses
  - RNA extraction and analyses
  - Protein extraction from tissues and quantification
  - Sample treatment and mass spectrometry of tissue-derived extracts
  - RNA fluorescence *in situ* hybridization and immunofluorescence
  - Bioinformatics analyses for putative circRNA-miRNA-mRNA networks
  - Absolute quantification
  - AGO2 crosslinking immunoprecipitation (CLIP) assay
  - Luciferase reporter plasmid construction
  - Luciferase assays
  - Native pull-down using striatal tissue extracts
  - Sample preparation and UV-crosslinked striatum pull-down
  - Open field test
  - Neuromuscular test
  - Contextual fear conditioning (CFC)
  - Calcium imaging recordings and data processing
- QUANTIFICATION AND STATISTICAL ANALYSIS

SUPPLEMENTAL INFORMATION

Supplemental information can be found online at https://doi.org/10.1016/j.celrep.2024.114766.

Received: January 9, 2024
Revised: August 6, 2024
Accepted: August 30, 2024

REFERENCES

1. D'Ambra, E., Capauto, D., and Morlando, M. (2019). Exploring the Regulatory Role of Circular RNAs in Neurodegenerative Disorders. Int. J. Mol. Sci. *20*, 5477. https://doi.org/10.3390/ijms20215477.
2. Ashwal-Fluss, R., Meyer, M., Pamudurti, N.R., Ivanov, A., Bartok, O., Hanan, M., Evantal, N., Memczak, S., Rajewsky, N., and Kadener, S. (2014). circRNA biogenesis competes with pre-mRNA splicing. Mol. Cell *56*, 55–66. https://doi.org/10.1016/j.molcel.2014.08.019.
3. Santos-Rodriguez, G., Voineagu, I., and Weatheritt, R.J. (2021). Evolutionary dynamics of circular RNAs in primates. Elife *10*, e69148. https://doi.org/10.7554/eLife.69148.
4. Rybak-Wolf, A., Stottmeister, C., Glažar, P., Jens, M., Pino, N., Giusti, S., Hanan, M., Behm, M., Bartok, O., Ashwal-Fluss, R., et al. (2015). Circular RNAs in the Mammalian Brain Are Highly Abundant, Conserved, and Dynamically Expressed. Mol. Cell *58*, 870–885. https://doi.org/10.1016/j.molcel.2015.03.027.
5. Szabo, L., Morey, R., Palpant, N.J., Wang, P.L., Afari, N., Jiang, C., Parast, M.M., Murry, C.E., Laurent, L.C., and Salzman, J. (2015). Statistically based splicing detection reveals neural enrichment and tissue-specific induction of circular RNA during human fetal development. Genome Biol. *16*, 126. https://doi.org/10.1186/s13059-015-0690-5.
6. Xia, S., Feng, J., Lei, L., Hu, J., Xia, L., Wang, J., Xiang, Y., Liu, L., Zhong, S., Han, L., and He, C. (2017). Comprehensive characterization of tissue-specific circular RNAs in the human and mouse genomes. Briefings Bioinf. *18*, 984–992. https://doi.org/10.1093/bib/bbw081.
7. You, X., Vlatkovic, I., Babic, A., Will, T., Epstein, I., Tushev, G., Akbalik, G., Wang, M., Glock, C., Quedenau, C., et al. (2015). Neural circular RNAs are derived from synaptic genes and regulated by development and plasticity. Nat. Neurosci. *18*, 603–610. https://doi.org/10.1038/nn.3975.
8. D'Ambra, E., Santini, T., Vitiello, E., D'Uva, S., Silenzi, V., Morlando, M., and Bozzoni, I. (2021). Circ-Hdgfrp3 shuttles along neurites and is trapped in aggregates formed by ALS-associated mutant FUS. iScience *24*, 103504. https://doi.org/10.1016/j.isci.2021.103504.
9. van Rossum, D., Verheijen, B.M., and Pasterkamp, R.J. (2016). Circular RNAs: Novel Regulators of Neuronal Development. Front. Mol. Neurosci. *9*, 74. https://doi.org/10.3389/fnmol.2016.00074.
10. Jia, E., Zhou, Y., Liu, Z., Wang, L., Ouyang, T., Pan, M., Bai, Y., and Ge, Q. (2020). Transcriptomic Profiling of Circular RNA in Different Brain Regions of Parkinson's Disease in a Mouse Model. Int. J. Mol. Sci. *21*, 3006. https://doi.org/10.3390/ijms21083006.
11. Aquilina-Reid, C., Brennan, S., Curry-Hyde, A., Teunisse, G.M., and The Nygc Als Consortium; and Janitz, M. (2022). Circular RNA Expression and Interaction Patterns Are Perturbed in Amyotrophic Lateral Sclerosis. Int. J. Mol. Sci. *23*, 14665. https://doi.org/10.3390/ijms232314665.
12. Gasparini, S., Del Vecchio, G., Gioiosa, S., Flati, T., Castrignano, T., Legnini, I., Licursi, V., Ricceri, L., Scattoni, M.L., Rinaldi, A., et al. (2020). Differential Expression of Hippocampal Circular RNAs in the BTBR Mouse Model for Autism Spectrum Disorder. Mol. Neurobiol. *57*, 2301–2313. https://doi.org/10.1007/s12035-020-01878-6.
13. Doxakis, E. (2022). Insights into the multifaceted role of circular RNAs: implications for Parkinson's disease pathogenesis and diagnosis. NPJ Parkinsons Dis. *8*, 7. https://doi.org/10.1038/s41531-021-00265-9.
14. Feng, Z., Zhang, L., Wang, S., and Hong, Q. (2020). Circular RNA circDLGAP4 exerts neuroprotective effects via modulating miR-134-5p/CREB pathway in Parkinson's disease. Biochem. Biophys. Res. Commun. *522*, 388–394. https://doi.org/10.1016/j.bbrc.2019.11.102.
15. Lukiw, W.J. (2013). Circular RNA (circRNA) in Alzheimer's disease (AD). Front. Genet. *4*, 307.
16. Dube, U., Del-Aguila, J.L., Li, Z., Budde, J.P., Jiang, S., Hsu, S., Ibanez, L., Fernandez, M.V., Farias, F., Norton, J., et al. (2019). An atlas of cortical circular RNA expression in Alzheimer disease brains demonstrates clinical

and pathological associations. Nat. Neurosci. *22*, 1903–1912. https://doi.org/10.1038/s41593-019-0501-5.

17. Chen, Y.-J., Chen, C.-Y., Mai, T.-L., Chuang, C.-F., Chen, Y.-C., Gupta, S.K., Yen, L., Wang, Y.-D., and Chuang, T.-J. (2020). Genome-wide, integrative analysis of circular RNA dysregulation and the corresponding circular RNA-microRNA-mRNA regulatory axes in autism. Genome Res. *30*, 375–391. https://doi.org/10.1101/gr.255463.119.
18. Zhou, M., Li, S., and Huang, C. (2024). Physiological and pathological functions of circular RNAs in the nervous system. Neural Regen. Res. *19*, 342–349. https://doi.org/10.4103/1673-5374.379017.
19. Errichelli, L., Dini Modigliani, S., Laneve, P., Colantoni, A., Legnini, I., Capauto, D., Rosa, A., De Santis, R., Scarfò, R., Peruzzi, G., et al. (2017). FUS affects circular RNA expression in murine embryonic stem cell-derived motor neurons. Nat. Commun. *8*, 14741. https://doi.org/10.1038/ncomms14741.
20. Chen, L.-L., Bindereif, A., Bozzoni, I., Chang, H.Y., Matera, A.G., Gorospe, M., Hansen, T.B., Kjems, J., Ma, X.-K., Pek, J.W., et al. (2023). A guide to naming eukaryotic circular RNAs. Nat. Cell Biol. *25*, 1–5. https://doi.org/10.1038/s41556-022-01066-9.
21. Colantoni, A., Capauto, D., Alfano, V., D'Ambra, E., D'Uva, S., Tartaglia, G.G., and Morlando, M. (2023). FUS Alters circRNA Metabolism in Human Motor Neurons Carrying the ALS-Linked P525L Mutation. Int. J. Mol. Sci. *24*, 3181. https://doi.org/10.3390/ijms24043181.
22. Cajigas, I.J., Tushev, G., Will, T.J., tom Dieck, S., Fuerst, N., and Schuman, E.M. (2012). The local transcriptome in the synaptic neuropil revealed by deep sequencing and high-resolution imaging. Neuron *74*, 453–466. https://doi.org/10.1016/j.neuron.2012.02.036.
23. Biever, A., Glock, C., Tushev, G., Ciirdaeva, E., Dalmay, T., Langer, J.D., and Schuman, E.M. (2020). Monosomes actively translate synaptic mRNAs in neuronal processes. Science *367*, eaay4991. https://doi.org/10.1126/science.aay4991.
24. Durkin, M.E., Yuan, B.-Z., Zhou, X., Zimonjic, D.B., Lowy, D.R., Thorgeirsson, S.S., and Popescu, N.C. (2007). DLC-1:a Rho GTPase-activating protein and tumour suppressor. J. Cell Mol. Med. *11*, 1185–1207. https://doi.org/10.1111/j.1582-4934.2007.00098.x.
25. Sabbir, M.G., Wigle, N., Loewen, S., Gu, Y., Buse, C., Hicks, G.G., and Mowat, M.R.A. (2010). Identification and characterization of Dlc1 isoforms in the mouse and study of the biological function of a single gene trapped isoform. BMC Biol. *8*, 17. https://doi.org/10.1186/1741-7007-8-17.
26. Shepherd, G.M.G. (2013). Corticostriatal connectivity and its role in disease. Nat. Rev. Neurosci. *14*, 278–291. https://doi.org/10.1038/nrn3469.
27. Lee, S.H., Lumelsky, N., Studer, L., Auerbach, J.M., and McKay, R.D. (2000). Efficient generation of midbrain and hindbrain neurons from mouse embryonic stem cells. Nat. Biotechnol. *18*, 675–679. https://doi.org/10.1038/76536.
28. Di Angelantonio, S., Bertollini, C., Piccinin, S., Rosito, M., Trettel, F., Pagani, F., Limatola, C., and Ragozzino, D. (2015). Basal adenosine modulates the functional properties of AMPA receptors in mouse hippocampal neurons through the activation of A1R A2AR and A3R. Front. Cell. Neurosci. *9*, 409. https://doi.org/10.3389/fncel.2015.00409.
29. Fucile, S., Miledi, R., and Eusebi, F. (2006). Effects of cyclothiazide on GluR1/AMPA receptors. Proc. Natl. Acad. Sci. USA *103*, 2943–2947. https://doi.org/10.1073/pnas.0511063103.
30. Morris, R.W., Quail, S., Griffiths, K.R., Green, M.J., and Balleine, B.W. (2015). Corticostriatal Control of Goal-Directed Action Is Impaired in Schizophrenia. Biol. Psychiatr. *77*, 187–195. https://doi.org/10.1016/j.biopsych.2014.06.005.
31. La-Vu, M., Tobias, B.C., Schuette, P.J., and Adhikari, A. (2020). To Approach or Avoid: An Introductory Overview of the Study of Anxiety Using Rodent Assays. Front. Behav. Neurosci. *14*, 145. https://doi.org/10.3389/fnbeh.2020.00145.
32. Ahmari, S.E., Spellman, T., Douglass, N.L., Kheirbek, M.A., Simpson, H.B., Deisseroth, K., Gordon, J.A., and Hen, R. (2013). Repeated cortico-striatal stimulation generates persistent OCD-like behavior. Science *340*, 1234–1239. https://doi.org/10.1126/science.1234733.
33. Dell'Orco, M., Sardone, V., Gardiner, A.S., Pansarasa, O., Bordoni, M., Perrone-Bizzozero, N.I., and Cereda, C. (2021). HuD regulates SOD1 expression during oxidative stress in differentiated neuroblastoma cells and sporadic ALS motor cortex. Neurobiol. Dis. *148*, 105211. https://doi.org/10.1016/j.nbd.2020.105211.
34. Eipper-Mains, J.E., Kiraly, D.D., Palakodeti, D., Mains, R.E., Eipper, B.A., and Graveley, B.R. (2011). microRNA-Seq reveals cocaine-regulated expression of striatal microRNAs. RNA *17*, 1529–1543. https://doi.org/10.1261/rna.2775511.
35. Enright, A.J., John, B., Gaul, U., Tuschl, T., Sander, C., and Marks, D.S. (2003). MicroRNA targets in Drosophila. Genome Biol. *5*, R1. https://doi.org/10.1186/gb-2003-5-1-r1.
36. Agarwal, V., Bell, G.W., Nam, J.-W., and Bartel, D.P. (2015). Predicting effective microRNA target sites in mammalian mRNAs. Elife *4*, e05005. https://doi.org/10.7554/eLife.05005.
37. Piwecka, M., Glažar, P., Hernandez-Miranda, L.R., Memczak, S., Wolf, S.A., Rybak-Wolf, A., Filipchyk, A., Klironomos, F., Cerda Jara, C.A., Fenske, P., et al. (2017). Loss of a mammalian circular RNA locus causes miRNA deregulation and affects brain function. Science *357*, eaam8526. https://doi.org/10.1126/science.aam8526.
38. Yu, H., Xie, B., Zhang, J., Luo, Y., Galaj, E., Zhang, X., Shen, Q., Liu, Y., Cong, B., Wen, D., and Ma, C. (2021). The role of circTmeff-1 in incubation of context-induced morphine craving. Pharmacol. Res. *170*, 105722. https://doi.org/10.1016/j.phrs.2021.105722.
39. Bicker, S., Lackinger, M., Weiß, K., and Schratt, G. (2014). MicroRNA-132, -134, and -138: a microRNA troika rules in neuronal dendrites. Cell. Mol. Life Sci. *71*, 3987–4005. https://doi.org/10.1007/s00018-014-1671-7.
40. Wayman, G.A., Davare, M., Ando, H., Fortin, D., Varlamova, O., Cheng, H.-Y.M., Marks, D., Obrietan, K., Soderling, T.R., Goodman, R.H., and Impey, S. (2008). An activity-regulated microRNA controls dendritic plasticity by down-regulating p250GAP. Proc. Natl. Acad. Sci. USA *105*, 9093–9098. https://doi.org/10.1073/pnas.0803072105.
41. Zimmerman, A.J., Hafez, A.K., Amoah, S.K., Rodriguez, B.A., Dell'Orco, M., Lozano, E., Hartley, B.J., Alural, B., Lalonde, J., Chander, P., et al. (2020). A psychiatric disease-related circular RNA controls synaptic gene expression and cognition. Mol. Psychiatr. *25*, 2712–2727. https://doi.org/10.1038/s41380-020-0653-4.
42. Sagot, B., Li, L., and Zhou, F.-M. (2018). Hyperactive Response of Direct Pathway Striatal Projection Neurons to L-dopa and D1 Agonism in Freely Moving Parkinsonian Mice. Front. Neural Circ. *12*, 57. https://doi.org/10.3389/fncir.2018.00057.
43. Kramer, M.C., Liang, D., Tatomer, D.C., Gold, B., March, Z.M., Cherry, S., and Wilusz, J.E. (2015). Combinatorial control of Drosophila circular RNA expression by intronic repeats, hnRNPs, and SR proteins. Genes Dev. *29*, 2168–2182. https://doi.org/10.1101/gad.270421.115.
44. Schneider, C.A., Rasband, W.S., and Eliceiri, K.W. (2012). NIH Image to ImageJ: 25 years of image analysis. Nat. Methods *9*, 671–675. https://doi.org/10.1038/nmeth.2089.
45. Kuo, H.-Y., and Liu, F.-C. (2019). Synaptic Wiring of Corticostriatal Circuits in Basal Ganglia: Insights into the Pathogenesis of Neuropsychiatric Disorders. eNeuro *6*, 0076–19.2019. https://doi.org/10.1523/ENEURO.0076-19.2019.
46. De Risi, M., Tufano, M., Alvino, F.G., Ferraro, M.G., Torromino, G., Gigante, Y., Monfregola, J., Marrocco, E., Pulcrano, S., Tunisi, L., et al. (2021). Altered heparan sulfate metabolism during development triggers dopamine-dependent autistic-behaviours in models of lysosomal storage disorders. Nat. Commun. *12*, 3495. https://doi.org/10.1038/s41467-021-23903-5.
47. Gu, Z., Eils, R., and Schlesner, M. (2016). Complex heatmaps reveal patterns and correlations in multidimensional genomic data. Bioinformatics *32*, 2847–2849. https://doi.org/10.1093/bioinformatics/btw313.

48. Mann, M., Wright, P.R., and Backofen, R. (2017). IntaRNA 2.0: enhanced and customizable prediction of RNA-RNA interactions. Nucleic Acids Res. *45*, W435–W439. https://doi.org/10.1093/nar/gkx279.

49. McGeary, S.E., Lin, K.S., Shi, C.Y., Pham, T.M., Bisaria, N., Kelley, G.M., and Bartel, D.P. (2019). The biochemical basis of microRNA targeting efficacy. Science *366*, eaav1741. https://doi.org/10.1126/science.aav1741.

50. Bolte, S., and Cordelières, F.P. (2006). A guided tour into subcellular colocalization analysis in light microscopy. J. Microsc. *224*, 213–232. https://doi.org/10.1111/J.1365-2818.2006.01706.X.

51. Desideri, F., D'Ambra, E., Laneve, P., and Ballarino, M. (2022). Advances in endogenous RNA pull-down: A straightforward dextran sulfate-based method enhancing RNA recovery. Front. Mol. Biosci. *9*, 1004746. https://doi.org/10.3389/fmolb.2022.1004746.

STAR★METHODS

KEY RESOURCES TABLE

REAGENT or RESOURCE	SOURCE	IDENTIFIER
Antibodies		
Rabbit polyclonal anti-PSD95	Cell Signaling Technology	cat# 25075; RRID:AB_561221
Anti-Beta III Tubulin	Sigma-Aldrich	cat# AB9354; RRID:AB_570918
Mouse monoclonal anti-GRIA1	Proteintech	cat# 67642-1-Ig; RRID:AB_2882842
Rabbit polyclonal anti-VGLUT2	Invitrogen	cat# 42-7800; RRID:AB_2533537
Donkey anti-Chicken 488A	Sigma-Aldrich	cat# SAB4600031; RRID:AB_2721061
Donkey anti-Rabbit Alexa Fluor™ 647	Invitrogen	cat# A-31573; RRID:AB_2536183
Donkey anti-Mouse Alexa Fluor™ 647	Thermo Fisher Scientific	cat# A32787; RRID:AB_2762830
Goat anti-Rabbit Alexa Fluor™ 488	Thermo FIsher Scientific	cat# A11008; RRID:AB_143165
Anti-Mouse HRP	Invitrogen	cat#32430; RRID:AB_1185566
Mouse monoclonal anti-AGO2	Sigma-Aldrich	cat# SAB4200724; RRID:AB_10794511
Mouse monoclonal anti-GAPDH (6C5)	Santa Cruz Biotechnology	cat# sc-32233; RRID:AB_627679
Normal mouse IgG	Santa Cruz Biotechnology	cat# sc-2025; RRID:AB_737182
Bacterial and virus strains		
Subcloning Efficiency DH5α Competent Cells	Invitrogen	cat#18265-017
MAX Efficiency DH5α Competent Cells	Invitrogen	cat#18258-012
Chemicals, peptides, and recombinant proteins		
1–ethyl–3–(3–dimethylaminopropyl) carbodiimide (EDC)	Sigma-Aldrich	cat# 800907
1-Methylimidazole	Sigma-Aldrich	cat# 805852
Levamisole Solution	Vector laboratories	cat# SP-5000-18
t-RNA	Roche	cat# 10109541001
Formamide	Sigma-Aldrich	cat# 47671
8% Paraformaldehyde aqueous solution	Electron Microscopy Sciences	cat# 157-8
Magnesium Chloride Hexahydrate	Electron Microscopy Sciences	cat# 18010
Vanadyl ribonucleoside complexes	Sigma-Aldrich	cat# 94740
Dextran sulfate sodium salt from Leuconostoc spp.	Sigma-Aldrich	cat# D8906
Red Substrate Kit, Alkaline Phosphatase (AP)	Vector Laboratories	cat# SK-5100
Anti-Digoxigenin-AP conjugate	Roche	cat# 11093274910
ProLong Diamond Antifade Mountant	Thermo Fisher Scientific	cat# P-36961
Goat Serum	Sigma-Aldrich	cat# G9023
DAPI	Sigma-Aldrich	cat# D9542
Dulbecco's Phosphate Buffered Saline w/o $MgCl_2$ and $CaCl_2$	Sigma-Aldrich	cat# D8537
Dulbecco's Phosphate Buffered Saline with $MgCl_2$ and $CaCl_2$	Sigma-Aldrich	cat# D8662

(*Continued on next page*)

Continued

REAGENT or RESOURCE	SOURCE	IDENTIFIER
Trypsin solution from porcine pancreas	Sigma-Aldrich	cat# T4549
Trypsin-EDTA Solution	Sigma-Aldrich	cat# T4299
EmbryoMax DMEM	Millipore	cat# SLM-220-B
Neurobasal™ Medium	Gibco	cat# 21103049
Advanced DMEM/F12	Gibco	cat# 12634010
Dulbecco's Modified Eagle's Medium/Nutrient Mixture F-12 Ham	Thermo Fisher Scientific	cat# D6421
DMEM-High Glucose	Sigma-Aldrich	cat# D6546
Sterile Earle's Balanced Salt Solution (EBSS)	Sigma-Aldrich	cat# E7510
Embryonic stem cell FBS, qualified, US origin	Gibco	cat# 16141-079
KnockOut™ Serum Replacement	Gibco	cat# 10828028
Fetal Bovine Serum, qualified, Brazil	Gibco	cat# 10270-106
Penicillin/Streptomycin	Sigma-Aldrich	cat# P0781
GlutaMAX™Supplement	Thermo Fisher Scientific	cat# 35050061
L-glutamine	Sigma-Aldrich	cat# G7513
Sodium Pyruvate	Thermo Fisher Scientific	cat# 11360070
EmbryoMax non-essential amino acids	Millipore	cat# TMS-001-C
EmbryoMax Nucleosides (100X)	Millipore	cat# ES-008-D
2-mercaptoethanol for ES cells	Millipore	cat# ES-007-E
N-2 supplement	Gibco	cat# 17502-001
ESGRO® Recombinant Mouse LIF Protein	Chemicon	cat# ESG11107
GSK-3 Inhibitor XVI	Sigma-Aldrich	cat# 361559
PD173074	Sigma-Aldrich	cat# P2499
L-ascorbic acid	Sigma-Aldrich	cat# TMS-001-C
Smoothened agonist, SAG	Sigma-Aldrich	cat# 566660
Recombinant mouse FGF-8b	Bio-Techne	cat# 423-F8-025
Recombinant human FGF basic (bFGF)	Bio-Techne	Cat# 233-FB-010
Papain	Worthington Biochemical Corporation	cat# LK003176
Ovomucoid inhibitor-Albumin	Worthington Biochemical Corporation	cat# LK003182
Deoxyribonuclease I from bovine pancreas	Sigma-Aldrich	cat# DN25
Poly-L-ornithine	Sigma-Aldrich	cat# P-3655
Laminin from Engelbreth-Holm-Swarm murine sarcoma basement membrane	Sigma-Aldrich	cat# L2020
Ultrapure Water with 0.1% Gelatin	Millipore	cat# ES-006-B
Fibronectin from human plasma	Sigma-Aldrich	cat# F2006
Opti-MEM™ Reduced Serum Medium	Thermo Fisher Scientific	cat# 31985070
Lipofectamine™ 2000 Transfection Reagent	Thermo Fisher Scientific	cat# 11668019
FastDigest XhoI	Thermo Fisher Scientific	cat# FD0694
FastDigest NotI	Thermo Fisher Scientific	cat# FD0594
10X FastDigest Green Buffer	Thermo Fisher Scientific	cat# B72
cOmplete™, EDTA-free Protease Inhibitor Cocktail	Roche	cat# 11873580001
T4 Polynucleotide Kinase	New England Biolabs	cat# M0201L
T4 DNA ligase	New England Biolabs	cat# M0202L
RiboLock RNase Inhibitor	Thermo Fisher Scientific	cat# EO0384
Dimethyl sulfoxide	Sigma-Aldrich	cat# D4540
Mytaq DNA polymerase	Bioline	cat# BIO-21105
CloneAmp™ HiFi PCR Premix	Clontech	cat# 639298

(*Continued on next page*)

Continued

REAGENT or RESOURCE	SOURCE	IDENTIFIER
PowerUp SYBR Green Master Mix	Life Technologies	cat# A25742
NuPAGE™ MOPS SDS Running Buffer (20X)	Invitrogen	cat# NP0001
Clarity™ Western ECL Substrate	Bio-Rad	cat# 1705061
NuPAGE 4–12% Bis-Tris Gel	Invitrogen	cat# NP0321
Amersham Protran 0.45 μm Nitrocellulose Blotting Membrane	Cytiva	cat# 10600002
Difco™ Skim Milk	BD Life Sciences	cat# 232100
4X Laemmli Sample Buffer	Bio-Rad	cat# 161-0747
Streptavidin MagneSphere Paramagnetic Particles	Promega	cat# Z5481
Dynabeads Protein G	Thermo Fisher Scientific	cat# 10004D
Proteinase K, recombinant PCR Grade	Roche	cat# 03115828001
AMPA	Sigma-Aldrich	cat# A6816
Doxycycline Hyclate	Sigma-Aldrich	cat# D5207
Puromycin (solution)	InvivoGen	cat# ant-pr-1
Cyclothiazide	Sigma-Aldrich	cat# C9847
Fluo4-AM, cell permeant	Invitrogen	cat# F14201
O.C.T. Compound Cryostat Embedding Medium	Scigen	cat# 4586
QIAzol Lysis Reagent	Qiagen	cat# 79306
Triton™ X-100	Sigma-Aldrich	cat# 9002-93-1
NP-40	Sigma-Aldrich	cat# 85124
Tween® 20	Sigma-Aldrich	cat# 1379
QIAcuity EG PCR Kit	Qiagen	cat# 250111
Critical commercial assays		
BaseScope™ Detection Reagent Kit v2	ACD	323910
RNAScope™ Pretreatment Reagents	ACD	322381
RNAScope™ Wash Buffer Reagents	ACD	cat#310091
Direct-Zol RNA MiniPrep Kit	Zymo Research	cat#R2050
miRNeasy Mini Kit	Qiagen	cat#217004
Quick-RNA™ Miniprep Kit	Zymo Research	cat#R1055
NucleoSpin Gel and PCR Clean-up	MACHEREY-NAGEL	cat# 740609.250
Plasmid DNA extraction Mini kit	Fisher Molecular Biology	cat# DE-035
NucleoBond Xtra Midi EF	MACHEREY-NAGEL	cat# 740420.50
Genomic DNA Extraction Kit mini	Geneaid Biotech Ltd.	cat # YGT100
In-Fusion® HD Cloning Kit	Takara Bio	cat# 102518
PrimeScript™ RT Reagent Mix	Takara Bio	cat#RR036b
Superscript™ Vilo cDNA Synthesis Kit	Invitrogen	cat# 11754050
miRCURY® LNA® RT Kit	Qiagen	cat# 339340
miRCURY® LNA® miRNA PCR Assay	Qiagen	cat# 339306
Pierce™ BCA protein assay kit	Thermo Fisher Scientific	cat# 23225
RNA Interactome MagIC Beads Kit	ElementZero Biolabs	N/A
Dual-Luciferase® Reporter Assay System	Promega	cat# E1960
Deposited data		
Raw and analyzed data	This paper	PRIDE database identifier: PXD054407
Experimental models: Cell lines		
Neuro-2a (N2a)	ATCC	cat# CCL-131
CF1 Mouse Embryonic Fibroblasts, irradiated	Gibco	cat# A34180

(*Continued on next page*)

Continued

REAGENT or RESOURCE	SOURCE	IDENTIFIER
Experimental models: Organisms/strains		
Mouse C57BL/6J WT	This paper	N/A
Mouse C57BL/6J, circDlc1(2)$^{-/-}$	This paper	N/A
Mouse C57BL/6J, Dlc1-206$^{-/-}$	This paper	N/A
Mouse C57BL/6J WT mESCs	This paper	N/A
Mouse C57BL/6J, circDlc1(2)$^{-/-}$ mESCs	This paper	N/A
Mouse C57BL/6J, Dlc1-206$^{-/-}$ mESCs	This paper	N/A
Mouse C57BL/6J, circDlc1(2)$^{-/-}$ Rescue mESCs	This paper	N/A
Oligonucleotides		
Oligonucleotides used for the genotyping in this work are listed in Table S2	This paper	N/A
Oligonucleotides for qPCR experiments in this work are listed in Table S2	This paper	N/A
Oligonucleotides for miRNA qPCR experiments in this work are listed in Table S3	Qiagen	cat# 339306
Oligonucleotides for plasmid construction are listed in Table S2	This paper	N/A
siRNAs used in this work are listed in Table S2	This paper	N/A
DNA oligonucleotide probes are listed in Table S2	This paper	N/A
miRCURY LNA miRNA Detection Probes mmu-miR-130b-5p mmu-miR-132-3p	EXIQON	cat# YD00615959-BCG YD00615938-BCG
Mm circ-Dlc1-specific probe for BaseScope™	ACD	cat# 708481
Recombinant DNA		
circDlc1(2) overexpression vector	This paper	N/A
circDlc1(2) Δ130 overexpression vector	This paper	N/A
psiCHECK™-2 Vector	Promega	cat# C8021
ZKSCAN1	Kramer et al., 2015[43]	Addgene plasmid #60649
pcDNA™3.1 (+) Mammalian Expression Vector	Thermo Fisher Scientific	cat# V79020
circDlc1(2)-WT	This paper	N/A
circDlc1(2)-mut	This paper	N/A
Gria1-WT-S	This paper	N/A
Gria1-mut-S	This paper	N/A
Gria1-WT-L	This paper	N/A
Gria1-mut-L	This paper	N/A
Gria1-ΔmiR	This paper	N/A
Grin2a-WT	This paper	N/A
Grin2a-mut	This paper	N/A
Software and algorithms		
ImageJ software	Schneider et al., 2012[44]	RRID:SCR_003070; https://imagej.nih.gov/ij/download.html
MetaMorph® Microscopy Automation and Image Analysis Software	Molecular Devices	RRID:SCR_002368; https://www.moleculardevices.com/products/cellular-imagingsystems/acquisitionand-analysissoftware/metamorph-microscopy#gref
ImageJ "3D viewer" plugin	Benjamin Schmid; ImageJ_3D_Viewer.jar	https://imagej.nih.gov/ij/plugins/3dviewer/
ImageJ "plot profile" plugin	N/A	https://imagej.net/ij/ij/docs/guide/146-30.html#toc-Subsection-30.11

(*Continued on next page*)

Continued

REAGENT or RESOURCE	SOURCE	IDENTIFIER
MetaFluor® Fluorescence Ratio Imaging Software	Molecular Devices	RRID:SCR_014294; http://www.moleculardevices.com/systems/metamorph-research-imaging/metafluor-fluorescence-ratio-imaging-software
Prism 9	GraphPad by Dotmatics	https://www.graphpad.com/scientific-software/prism/
QuantStudio 3 and 5 Real-Time PCR System Software	Thermo Fisher Scientific	RRID:SCR_020238; https://www.thermofisher.com/it/en/home/global/forms/life-science/quantstudio-3-5-software.html
miRanda software (v3.3a)	Enright et al., 2003[35]	RRID:SCR_017496; https://cbio.mskcc.org/miRNA2003/miranda.html
ComplexHeatmap	Gu et al., 2016[47]	RRID:SCR_017270; https://bioconductor.org/packages/release/bioc/html/ComplexHeatmap.html
IntaRNA 2.0	Mann et al., 2017[48]	https://github.com/BackofenLab/IntaRNA
Image Lab™ Software	N/A	RRID:SCR_014210; http://www.bio-rad.com/en-us/sku/1709690-image-lab-software
TargetScan (v8.0)	McGeary et al., 2019[49]	https://www.targetscan.org/mmu_80/
ImageJ "JACoP (Just Another Colocalization Plugin)" plugin	Bolte and Cordelieres, 2006[50]	https://imagej.nih.gov/ij/plugins/track/jacop.html

EXPERIMENTAL MODEL AND SUBJECT DETAILS

Generation of mouse lines

The mice were housed in the animal facility of EMBL Monterotondo at the Gene Editing and Embryology Facility (GEEF). Mice were maintained in temperature and humidity-controlled condition with food and water provided *ad libitum* and on 12-h light–dark cycle (light on at 7:00). They were housed in IVC Thoren racks in groups of 4 mice/cage. All experiments were approved by the Italian Ministry of health (approval n.82945.56) and conducted within the animal welfare regulations and guidelines. Both circ-KO and lin-KO mice were generated using CRISPR/Cas9 editing technology in C57BL/6J zygotes. crRNA oligos and tracrRNA were annealed and combined with a homology flanked ssODN (single stranded donor) coding for the desired mutation.

For the circ-KO mice, annealed single guide RNAs (sgRNAs) targeting the exon 1-intron 1 boundary (5′-TTGGCGGTAACAG CAACTCC-3'; 5′-AGGAGTTGCTGTTACCGCCA-3′) and the intron 1-exon 2 boundary (5′-TTCTTTCACAGTGGACAACA-3'; 5′-ACT CAAAGGGATGGAAGTCG-3′) of the *Dlc1* gene were complexed with Cas9 protein and combined with a 163 nt ssODN for the complete removal of intron 1. The ssODN was composed of asymmetrical homology arms corresponding to the perfect fusion of exons 1 and 2. For the lin-KO mice, sgRNAs targeting the fourth exon of *Dlc1* (5′-CCGATCCATCATCCACTCCA-3'; 5′-AGTAGGT GAGGTCCCTCGTT-3′) were used, together with a 450 nt-long ssODN comprised by asymmetrical homology arms and 100 nt of a minimal synthetic poly-A signal, followed by two repetitions of the polymerase destabilizing MAZ sequences. All single-stranded DNA and RNA oligos were synthesized by IDT. The Cas9 protein, sgRNA and ssDNA donor template (Cas9 protein 50 ng/μL, sgRNA 20 ng/μL, ssODN 10 ng/μL) were co-microinjected into zygote pronuclei using standard protocols and after overnight culture 2-cell embryos were surgically implanted into the oviduct of day 0.5 post-coitum pseudopregnant CD1 mice. Successful editing was validated by PCR genotyping using MyTaq DNA Polymerase (Bioline). gDNA extraction from tail biopsies was performed using the Genomic DNA Extraction kit (Geneaid Biotech Ltd.) according to the manufacturer's protocol. Oligonucleotide primers are listed in Table S2. A founder F0 male was selected and backcrossed with wild-type mice to generate F1. The KO lines were maintained by heterozygous vs. heterozygous crosses.

Cell culture conditions and treatments

mESC culture

mESCs derived from C57/J WT, circ-KO and lin-KO mouse blastocysts were cultured as described in D'Ambra et al.[8] Briefly, cells were cultured on 0.1% gelatin-coated (Millipore) or MEF-coated (Gibco) dishes and maintained in mESC medium (Embryomax DMEM (Millipore), 15% Fetal Bovine Serum for ES (Gibco), 1X GlutaMAX (Thermo Fisher Scientific), 1X non-essential amino acids

(Millipore), 1X nucleosides (Millipore), 1X 2-mercaptoethanol (Millipore) and 1X Pen/Strep) supplemented with LIF (10^3 unit/mL, Chemicon), PD173074 (1.5 μM, Sigma-Aldrich) and Gsk-3i (1.5 μM, Sigma-Aldrich) (LIF+2i condition).

Generation of the inducible circ-Dlc1(2) *rescue (circ-OE) mESC line*

Circ-KO mESCs were plated onto 0.1% gelatin-coated plates for at least two passages. 1.9 x 10^5 cells were plated on 60 mm plates 24 h prior to transfection. For the transfection, cells were incubated for 6 h with: 1 μg piggyBAC transposon vector containing the second exon of *Dlc1* together with 1500 bp of the up- and downstream flanking introns and a puromycin selection cassette, 125 ng of helper transposase, 3.5 μL of Lipofectamine 2000 Transfection Reagent (Thermo Fisher Scientific) and up to 2 mL with Opti-MEM Reduced Serum Medium (Thermo Fisher Scientific). After 2 days, 0.75 μg/mL puromycin (InvivoGen) was added to the cell medium for the selection of cells with the successful integration of the cassette, which lasted for ~10 days (circ-OE mESCs).

Differentiation of mESCs to a terminally differentiated dopaminergic/glutamatergic neuronal population

Neuronal differentiation containing different neuron sub-types including dopaminergic neurons, was obtained following the Lee et al.[27] protocol with some adjustments. Before starting the differentiation, ES cells were plated for at least 1 passage on 0.1% gelatin-coated plates. The first day of differentiation ES cells were dissociated (0.25% trypsin–EDTA, Sigma-Aldrich) to single cells, and 5 × 10^5 cells were seeded into bacterial-grade dishes (10 mL) for serum-free suspension culture with ADNFK medium (composed by (1:1) Advanced DMEM/F12 (Gibco):Neurobasal medium (Gibco), 10% KnockOut Serum Replacement (Gibco), 1% GlutaMAX, 1% 2-mercaptoethanol, 1% Pen/Strep). Medium was changed to fresh ADNFK differentiation medium on day 3. On day 5, floating spheres were plated *en bloc* on dishes coated with poly-L-ornithine (Sigma-Aldrich) and Murine Laminin 20 μg/mL (Sigma-Aldrich). Cells were maintained 5–7 days in N2/neurobasal differentiation medium (Neurobasal/F12 (1:1), N2 (1/100, Gibco), 1% GlutaMAX, 1% sodium pyruvate (Thermo Fisher Scientific), 0.5% Pen/Strep, 1% non-essential amino acids) supplemented with Fibronectin 0.250 mg/mL (Sigma-Aldrich). When neural precursor migration out of aggregates was evident, cells were switched to N2/neurobasal medium supplemented with bFGF (10 ng/mL, Bio-Techne), FGF8 (100 ng/mL, Bio-Techne), SAG (0.25 μM, Sigma-Aldrich) and 2 μg/mL laminin. After four days bFGF was removed and substituted with Ascorbic Acid (200 μM, Sigma-Aldrich) and neurons were kept in this medium (refreshed every other day) for another 10–13 days for neuronal maturation. After plating the EBs, the media was changed every other day.

For *circDlc1(2)* rescue experiments, 100 ng/mL doxycycline (Sigma-Aldrich) was added to ADNFK medium upon differentiation induction, and to N2/neurobasal differentiation medium, every time the medium was refreshed.

N2a cell line

Murine neuroblastoma cells line, (N2a, ATCC) were cultured in DMEM-High Glucose medium (Sigma-Aldrich) with 10% Fetal Bovine Serum (Sigma-Aldrich), 100 mM L-glutamine (Sigma-Aldrich) and 100 mM Penicillin/Streptomycin (Sigma-Aldrich). 1.5-2 x 10^5 cells plated in 12-well multiwell plates were transiently cotransfected the following day, with 20 ng of the luciferase reporter plasmids and either mimics, LNAs, siRNAs or OE plasmids, using 1.25 μL Lipofectamine 2000 Transfection Reagent (Thermo Fisher Scientific) and 200 μL Opti-MEM Reduced Serum Medium (Thermo Fisher Scientific; overnight incubation) and 800 μL DMEM medium or 500 μL Opti-MEM (5 h over-day incubation) per well. For the mimics, 5 nM control mimic (Unspecific_AllStars_1 (SI03650318)) or miR-130b-5p mimic (Qiagen, miScript miRNA Mimic (MSY0004583) sequence: 5′-ACUCUUUCCCUGUUGCACUACU-3′). For the LNA assay, N2a cells were transfected with 50 nM control LNA (miRCURY LNA miRNA Inhibitor Control, 339136) or LNA against miR-130b-5p (miRCURY LNA miRNA Inhibitor, 339132, sequence: 5′-TAGTGCAACAGGGAAAGAG-3′), as above. *CircDlc1(2)* downregulation was obtained with an siRNA customly designed to target the back-splicing junction of *circDlc1(2)*, and modified accordingly (OnTargetPlus technology, Dharmacon, CTM-691810 Sense: 5′ CGCAAGAGAAAGUGGACAAUUUU). For the specific downregulation of *lin-Dlc1* (*Dlc1-206*), siRNAs were custom designed to target the isoform's exon 4 (OnTargetPlus technology, Dharmacon, CTM-943692 Sense: 5′ CCAACUAGACCAAGACAUAUU; CTM-943694 Sense: 5′ GAGCAAUUCUGGAACCAAAUU). *CircDlc1(2)* up-regulation was obtained by plating 1.5-2 x 10^5 N2a cells and transfecting them after 24 h with 300 ng of *circDlc1(2)* OE plasmid using 1.25 μL Lipofectamine 2000 Transfection Reagent and 200 μL Opti-MEM (overnight incubation) and 800 μL DMEM medium or 500 μL Opti-MEM (5-h over-day incubation). As control for circDlc1(2) OE experiments it was used an empty plasmid-coding DNA (pcDNA).

METHOD DETAILS

Mouse tissue collection for molecular analyses

Mice were weighed and then sacrificed by cervical dislocation. Relevant tissues were snap frozen in liquid nitrogen and stored at −80°C. Prior to protein and RNA extraction, tissues were ground to a powder using a pestle and mortar pre-chilled with liquid nitrogen. During grinding, liquid nitrogen was occasionally added to prevent the tissue from thawing. Ground tissues were then separated equally between two pre-chilled Eppendorf tubes, one destined for protein extraction and the other for RNA which were snap frozen again and stored at −80°C.

RNA extraction and analyses

QIAzol Lysis Reagent (Qiagen) was added to each Eppendorf tube containing the samples; RNA was isolated using the miRNeasy Mini Kit (Qiagen), Directzol RNA MiniPrep Kit (Zymo Research) or the Quick-RNA Miniprep Kit (Zymo Research) with on-column DNAse treatment, according to the manufacturer's instructions. If RNA was extracted from tissue, additional initial steps were added

to the procedure: 700 μL of QIAzol Lysis Reagent was added to each Eppendorf tube containing the tissue powder. The samples were readily vortexed for ~5–10 min until disrupted and homogenized. These were then centrifuged at 12,000xg for 10 min at 4°C. The supernatant was transferred to a new Eppendorf tube before proceeding with the standard extraction protocol. RNA was quantified using a NanoDrop 1000 Spectrophotometer (Thermo Fisher Scientific) before being reverse transcribed using the SuperScript VILO cDNA Synthesis Kit (Invitrogen), the PrimeScript RT Reagent Kit (Takara Bio USA) or the miRCURY LNA RT Kit (Qiagen). CDNAs were then diluted to a concentration of 1–2.5 ng/μL (when analyzing gene expression) or isovolumic with the input (when assessing target enrichments in pull-down or IP experiments) then stored at −20°C.

For RNA expression analyses, real-time PCR (qRT-PCR) was performed using PowerUp SYBR Green Master Mix (Life Technologies) on a 7500 Fast Real-Time PCR (Applied Biosystem) or QuantStudio 3 Real-Time PCR (Thermo Fisher Scientific). For the detection of miRNAs, qRT-PCR was performed using the miRCURY LNA miRNA PCR Assay (Qiagen) with Snord110 (Small Nucleolar RNA, C/D Box 110) as the internal control. Oligonucleotide primers used for qRT-PCR are listed in Tables S2 and S3.

Protein extraction from tissues and quantification

Tissues destined to protein extraction were weighed using a milligram balance. 500 μL of protein buffer (50 mM Tris, 5 mM EDTA, 150 mM NaCl, 10% glycerol, 21.5 mM $MgCl_2$, 1% Triton X-100 (Sigma-Aldrich) supplemented with 1X protease inhibitor cocktail (PIC, Roche) and 0.2 U/μL RiboLock RNase inhibitor (Thermo Fisher Scientific) was added per 100 mg of ground tissue powder. Tissues were then gradually homogenized using TissueRuptor II (Qiagen). Samples were centrifuged at 13,000 x g for 10 min at 4°C. The supernatant was collected and quantified with the Bradford colorimetric reaction (Bio-Rad).

Sample treatment and mass spectrometry of tissue-derived extracts

50 μg of protein extract was analyzed per tissue per animal. Disulphide bonds were first reduced by adding 10 μL of 100 mM dithiothreitol (DTT) and cysteine residues were alkylated by adding 30 μL of 100 mM Iodoacetamide. Samples were then digested into peptides through the addition of 1 μg of Trypsin. Digested peptides were dried, resuspended in 50 μL of 3% acetonitrile added with 0.1% formic acid and analyzed on a Thermo Exploris 480 Orbitrap, coupled with a Dionex Ultimate 3000 nano-LC system. Both systems were purchased by Thermo Fisher Scientific. Peptides were separated in a linear gradient, using water and acetonitrile (added with 0.1% formic acid): Injection volume was 0.5 μL, flow was 0.300 μL/min, the column temperature was 40°C, samples were eluted with the following gradient program: 0.0–5.0 min 3% B; 5.0–41.0 min 3 to 19% B; 41.0–55.0 min 19 to 29% B; 55.0–65.0 min 29 to 41% B; 65.0–66.0 min 41 to 95% B; 96.0–76 min 95%B and 76.0–77 min back to 3% B. The column was then reconditioned for 13 min. The total run time was 90 min. Peptides were analyzed in positive ESI mode, with a capillary voltage set to 2.0 kV. The RF lens was set to 40% and the AGC target was set to 300%. Data acquisition was performed in Data Independent mode (DIA) with a survey scan set from 400 to 1000 m/z at 120000 resolution. MS/MS spectra were acquired in HCD mode with the collision energy set to 30%. Data analysis was carried out using the Spectronaut software (Biognosys) and searching all RAW data against a Mus Musculus revised FASTA database downloaded from UNIPROT. Only proteins identified across all runs with at least 2 peptides and 1% FDR were considered. Proteins identified by only one single peptide hit were excluded from the analysis. The Bonferroni multiple test correction was applied to the observed abundances of the identified proteins. An arbitrary threshold of +/− 30% change in protein expression compared to the WT group was considered as significant. Functional enrichment analysis of the differentially expressed genes derived from mass spectrometry analysis of WT and circ-KO striatum-derived extracts was performed using the reactome pathway database.

RNA fluorescence *in situ* hybridization and immunofluorescence

Whole brain cryosections

Adult WT mice were sacrificed by cervical dislocation. The whole brain was dissected and readily fixed in 4% paraformaldehyde (PFA; Electron Microscopy Sciences; in PBS with Ca^{2+} and Mg^{2+}) for 48 h at 4°C on a rocking oscillator. The brain was then cryoprotected via a sucrose gradient (10, 20 and 30% in PBS with Ca^{2+} and Mg^{2+}), supplemented with 1:200 vanadyl ribonucleoside complexes (VRC; Sigma-Aldrich). The concentration of sucrose was increased upon tissue sinking. The tissue was then embedded in optimal cutting compound (OCT; Scigen) using liquid nitrogen-cooled (at least −80°C) 2-methylbutane. The excess liquid was removed with a paper towel prior to this procedure. 30 μm-thick sagittal whole brain tissue cryosections were obtained using a cryostat (Leica) set at −20°C, then stored at −80°C. On the day of the RNA-FISH, sections were thawed at RT and washed with 1X PBS for 5 min, oscillating the slides to remove the OCT. Slides were immersed and post-fixed in pre-chilled 4% PFA (in 1X PBS) for 10 min at 4°C. The tissue was dehydrated by sequentially immersing the slides in 50%, 70% and 100% EtOH, for 5 min at each percentage and at RT. The slides were then air-dried for 5 min at RT before undergoing the standard Basescope (Advanced Cell Diagnostics, BioTechne) protocol for fixed frozen tissue sections (ACD technical note n° 320534 and 323900). Probes used to detect *circDlc1(2)* (ref. 708481) were custom produced by Advanced Cell Diagnostics and designed to specifically target the back-splicing junction of the circular RNA. After chromogenic signal development of the FISH, the nuclei were counterstained with DAPI solution (1 μg/mL/PBS; Sigma-Aldrich) for 5 min at RT and then the coverslips were mounted using ProLong Diamond Antifade Mountant (Thermo Fisher Scientific). Images were acquired with an Olympus IX73 microscope equipped with a Crestoptics X-LIGHT V3

spinning disk system and a Prime BSI Express Scientific CMOS camera, using a 30X silicon objective (NA 1.05). The final image mosaic was obtained with the scan slide application of the MetaMorph software and for the images shown in the panels were applied ImageJ filter "maximum" for better visualization of the signal.

mESC-derived neurons

Cells cultured on pre-coated glass coverslips (0.01% poly-L-ornithine, 20 μg/mL laminin) were fixed in 4% PFA/4% sucrose/5mM $MgCl_2$/PBS (Electron Microscopy Sciences) for 30 min at 4°C and then stored in PBS/4% sucrose/1:100 VRC (Sigma-Aldrich) until use. For IF, cells were permeabilized (0.1% TritonTM X-100/2% BSA/PBS) for 45 min at room temperature and then incubated with anti-GRIA1 (67642-1-Ig, Proteintech) and anti-VGLUT2 (42–7800, Invitrogen) primary antibodies overnight at 4 °C. Subsequently, they were incubated with secondary antibodies (donkey anti-mouse Alexa Fluor 647, A32787 and goat anti-rabbit Alexa Fluor 488, A11008, both Thermo Fisher Scientific) diluted 1:200 in 2% BSA/PBS for 1h at room temperature. After washing with 0.1% Tween 20/PBS the cells were incubated with DAPI solution for 5 min at RT and then mounted using ProLong Diamond Antifade Mountant.

miRNA FISH

An additional fixation step was performed with 0.16M 1–ethyl–3–(3–dimethylaminopropyl) carbodiimide (EDC) dissolved in Methylimidazole buffer (0.13M 1-Methylimidazole/0.03 M NaCl/H_2O) for 30 min at RT. Cells were then permeabilized with Triton X-100 (0.2% Triton X-100/2mM VRC/PBS) for 5 min on ice. Before the *in situ* hybridization staining, IF for PSD-95 (1:200 in PBS; 25075, Cell Signaling Technologies) and beta Tubulin III (1:200 in PBS; AB9354, Sigma-Aldrich) was performed overnight at 4 °C. Finally, the secondary antibodies were incubated: Donkey anti-Chicken 488A antibody (SAB4600031, Sigma-Aldrich) and Donkey anti-Rabbit Alexa Fluor 647 (A-31573, Invitrogen) diluted 1:200 in 1% BSA/PBS for 45 min at RT. Before probe incubation, the cells were fixed with 4% PFA for 10 min at RT and incubated in pre-Hybridization Buffer (4X SSC/25% Formamide/2 mM VRC/H_2O) for 15 min at RT. Finally, 250 nM of miR-130b-5p or miR-132-3p LNA-probes were added to the cells in Hybridization Buffer (4X SSC/10% dextran sulfate/250 μg/mL tRNA/2 mM VRC/H_2O) 1h at 37°C. After stringent washes (1X SSC and 0.2X SSC/2% BSA) at 37°C, Digoxigenin was detected with Red Substrate Kit Alkaline Phosphatase (Vector Laboratories) according to the manufacturer's instructions. After extensive washing with H_2O, the cells were incubated with DAPI solution for 5 min at RT and then mounted using ProLong Diamond Antifade Mountant.

circDlc1(2) *FISH*

Detection of *circDlc1(2)* was performed via Basescope assay (Advanced Cell Diagnostics, Bio-Techne) as previously described in D'Ambra et al.[8] Samples were imaged using an inverted confocal Olympus IX73 microscope equipped with a Crestoptics X-LIGHT V3 spinning disk system and a Prime BSI Express Scientific CMOS camera and with an Olympus iX83 FluoView1200 laser scanning confocal microscope. The acquisitions were obtained using a UPLANSApo 60X (NA 1.35) oil objective collected with the MetaMorph software (Molecular Devices). The z stack confocal microscopy images were taken automatically (200 nm Z-spacing) and merged with the maximum intensity projection method.

Image analysis on cell samples

All the post-acquisition analysis were performed on MIP (Maximum Intensity Projection) from focal planes of the cells positive for TUBB3. FISH signal-scattering quantification was computed as the mean percentage of spots fraction located in neurites with respect to the total (FISH spots in the soma+neurite), while FISH spot areas were defined with the "analyze particle" plugin after binarization of the image. The ratio of FISH signals overlapping PSD-95 protein was expressed with Manders' Overlap Coefficient (MOC) using the co-localization tool (JaCoP plug-in). Line-scan analyses were performed on maximum projection of the Z-planes by using the "plot profile" plugin.

Bioinformatics analyses for putative circRNA-miRNA-mRNA networks

miRNAs expressed in the striatum were retrieved from Dell'Orco et al.[33] and Eipper-Mains et al.[34] selecting only miRNAs expressed more than 1 CPM (average expression). For the Dell'Orco et al.[33] dataset, an additional filter was imposed selecting miRNAs labeled as "High confidence". miRNA binding site predictions were performed using the miRanda software (v3.3a)[35] setting the minimum prediction score to 140 and the energy threshold at −15 kcal/mol. In order to reduce sequence redundancy, the longest functional isoform was selected as the representative for each gene. Annotated 3′UTR regions (ensemble 99) were used to assess miRNA binding to mRNAs. By performing the luciferase assay on the *Gria1* 3′UTR, we found that the mutation of the optimal interaction site of miR-130b-5p was not sufficient to abolish the responsiveness of the construct, thus we investigated the presence of other suboptimal interaction sites, identifying a second one (with −12.18 kcal/mol energy) lowering the miRanda energy threshold from −15 to −7 kcal/mol and additional miRNA-target predictions were performed using TargetScan v8.0.[36]

The heatmap representation performed using ComplexHeatmap[47] was used to summarize miRNA binding sites to circRNAs and mRNA targets. RNA-RNA interaction predictions were performed using the IntaRNA 2.0 software.[48] For both interaction predictions, in order to include the BSJ in the analysis, the *Dlc1* exon 2 sequence was extended by 50 nt, repeating the 5′ portion of the exon.

The control RNAs for the specificity of predicted interactions between *circDlc1(2)* and the mRNAs related to proteins with altered expression in the circ-KO mouse compared to the WT condition were selected with a custom Python script using length and structure information related to the representative isoform for each gene and retrieved from Ensemble 99. The prediction of the 5 most thermodynamically favorable interacting regions between *circDlc1(2)* and each target RNA was performed using the intaRNA2.0 parameter -n 5. Length normalization was carried out according to the intaRNA2.0 guidelines by dividing the energy of each interaction by

the natural logarithm of the target RNA length (nucleotides), omitting normalization for the length of the query circRNA as it is common to all predictions.

Absolute quantification

RNA samples used for the absolute quantification of the different RNA species were obtained from WT mESC-derived neurons at day 15. Digital PCR (dPCR) was performed using QIAcuity EG PCR Kit (Qiagen) on a 5-plex QIAcuity One device, (Qiagen) according to manufacturer's instructions. The following parameters were set for the imaging profile: 500 ms exposure duration and gain 6; in the case of saturation, the exposure duration was reduced by 30%.

AGO2 crosslinking immunoprecipitation (CLIP) assay

mESC-derived neuronal cells were UV-crosslinked at 4000 × 100 μJ/cm^2 and lysed with NP40-lysis buffer (50 mM Tris-HCl pH 7.5, 150 mM KCl, 2 mM EDTA, 1 mM NaF and 0.5% NP-40; Sigma-Aldrich) complemented with 0.5 mM DTT, 1X PIC and 0.2 U/μL Ribolock: they were placed on a tube rotator at 4°C for 10 min and then centrifuged at 13,000 x g for 15 min at 4°C. Clarified extracts were quantified using the Bradford assay. 1 mg of extract and 30 μL of Dynabeads Protein G (Thermo Fisher Scientific) were used for each IP (AGO2 or mouse IgG). The beads were washed twice with 1 mL of PBS-T (PBS without Ca^{2+} and Mg^{2+}/0.02% Tween 20 (Sigma-Aldrich)) and resuspended in 810 μL PBS-T. 400 μL of this bead suspension was added to 2 Eppendorf tubes which were then coated with 10 μg of antibody against AGO2 (SAB4200724; Sigma-Aldrich) or mouse IgG (sc-2025; Santa Cruz). The tubes were placed on a tube rotator for 2 h at RT. After the coating, beads were washed twice with PBS-T to remove excess antibodies. Before the addition of the extract, 10% of the volume (100 μg) was taken as the input. The remaining volume was divided between the two IP tubes which, together with the input, were placed back on the tube rotator for an overnight incubation at 4°C. The following day, the IP samples were washed thrice with 1 mL High salt buffer (50 mM Tris-HCl pH 7.5, 500 mM KCl and 0.05% NP-40) complemented with 0.5 mM DTT. For each wash, the beads were placed on a tube rotator for 1 min at RT. Beads were finally resuspended in 100 μL of complemented NP-40-lysis buffer. The input was also made up to the same final volume. For all samples, ¼ of the volume (25 μL) was transferred to a different Eppendorf tube corresponding to the protein fraction. The remaining $^3/_4$ were destined for RNA extraction (RNA fraction). 125 μL of proteinase K buffer 2x (200 mM Tris-HCl pH 7.5, 300 mM NaCl, 25 mM EDTA and 2% SDS) together with 50 μL of proteinase K (4 mg/mL final concentration; Roche) were added to the RNA fraction (remaining 75 μL) of each IP and 10% input sample. Samples were incubated for 30 min at 50°C and 600 RPM. Three volumes of QIAzol Lysis Reagent were added to each sample. IP samples were vortexed for 15 s prior to bead removal and were then removed with a magnetic rack. The supernatant was transferred to a new Eppendorf tube and stored at −20°C.

The protein fraction was assessed first, to ensure that AGO2 was successfully immunoprecipitated. 10 μL of 4x Laemmli Sample Buffer (Bio-Rad) and 50 mM DTT were added to each protein fraction (input and IP). These were heated at 90°C for 5 min; beads were then removed from the IP samples using a magnetic rack. Samples were loaded onto a precast NuPAGE 4–12% Bis-Tris 1.0 mm Mini Protein gel (Invitrogen) run for 1–1.5 h at 150 V using MOPS SDS running buffer (Invitrogen). Blotting was performed onto an Amersham Protran 0.45 mm nitrocellulose blotting membrane (Cytiva) in Tris-Glycine buffer (25 mM Tris, 192 mM glycine and 20% methanol), using a Mini Trans-Blot Electrophoretic Transfer Cell (Bio-Rad). The immunoblots were blocked with 5% Difco skimmed milk (BD Life Sciences)/TBS-T for 30 min and then incubated with primary antibodies for AGO2 (1:500, SAB4200724; Sigma-Aldrich) or GAPDH (1:1000, sc-32233; Santa Cruz), also diluted in 5% skimmed milk/TBS-T overnight at 4°C. The immunoblots were then incubated with anti-mouse HRP (1:10,000; 32430, Invitrogen) secondary antibody diluted in 5% skimmed milk/TBS-T for 1 h at RT prior to image acquisition. The immunoblots were incubated with Clarity Western ECL Blotting Substrate (Bio-Rad) and acquired using the ChemiDoc MP System (Bio-Rad). Images were analyzed using Image Lab Software (Bio-Rad). RNA from IP samples was finally isolated using the RNeasy Mini Kit with on-column DNAse treatment, according to the manufacturer's instructions (Qiagen).

Luciferase reporter plasmid construction

For the Luciferase assays, the 3′UTR of *Gria1* and *Grin2a*, and the exon 2 sequence of *Dlc1-206* were cloned downstream the Renilla reporter gene in psiCHECK-2 Vector (Promega) using XhoI and Not1 FastDigest restriction enzymes (Thermo Fisher Scientific). The vector (opened by inverse PCR) and inserts were amplified with CloneAmp HiFi PCR Premix (Clonetech) and oligonucleotides indicated in Table S2. The cloning was achieved with the In-Fusion HD Cloning Kit (Takara Bio). All the mutant constructs were obtained by inverse PCR followed by phosphorylation with T4 Polynucleotide Kinase (New England Biolabs) and self-ligation of the PCR product with T4 DNA ligase (New England Biolabs). For the *circDlc1(2)* overexpression the *circDlc1(2)* sequence was cloned in the circRNA mini vector ZKSCAN1,[43] addgene #60649, via the In-fusion strategy.

Luciferase assays

N2a cells were harvested and lysed 48 h after transfection, and Renilla luciferase (RLuc) and Firefly luciferase (FLuc) activities were measured by Dual-Luciferase Reporter Assay System (Promega) (50 μL per injector, 2 s delay, speed 200 μL/s). The FLuc gene contained in the reporter plasmids was used to normalize for transfection efficiency. Ratios of RLuc readings to FLuc readings (RLuc/FLuc) were taken for each experiment and normalized with respect to each respective control.

Native pull-down using striatal tissue extracts

250 μL of Lysis buffer (50 mM Tris-HCl pH 7.5, 150 mM NaCl, 3 mM $MgCl_2$, 0.5% NP40 and 2 mM EDTA) complemented with 1 mM DTT, 1X PIC and 0.2 U/μL Ribolock were added to previously ground striatum tissue powder which was then homogenized using the TissueRuptor II (Qiagen). Samples were centrifuged at 15,000xg for 15 min at 4°C. The supernatant was collected for quantification via the Bradford assay. 2 mg of cleared extract was collected for each pull-down condition (*circDlc1(2)* or *lacZ*) and then diluted by adding two volumes of Hybridization buffer (HB; 100 mM Tris-HCl pH 7.5, 300 mM NaCl, 1 mM $MgCl_2$, 0.2%, SDS, 15% Formamide, 0.5% NP-40 and 10 mM EDTA) complemented with 1 mM DTT, 1X PIC and 0.2 U/μL Ribolock. 200 μg of extract were collected corresponding to 10% of the input before adding dextran sulfate salt (DSS; Sigma-Aldrich) to each pull-down sample at a final concentration of 2.5%.[51] 5′-biotinylated 20 nt-long antisense DNA oligonucleotide probes (Sigma-Aldrich; 100 pmol/mg of extract) targeting *circDlc1(2)* or bacterial *lacZ* (control) (listed in Table S2) were diluted to a final volume of 50 μL in HB. These were denatured for 2 min at 80°C then added to each pull-down sample. The probes were incubated with the extract at 4°C on a tube rotator for 4 h, in parallel with the input sample. Prior to the end of incubation, 200 μL of Streptavidin MagnaSphere Paramagnetic Particles (Promega; 100 μL/mg of extract) were washed twice with HB using a magnetic rack. Beads were then resuspended in HB and 100 μL of bead suspension was transferred to each pull-down sample. The samples underwent an hour of incubation with the beads on a tube rotator at RT. The beads were then washed 4 times with HB, each time placing the samples on a tube rotator for 3 min at RT. Once the buffer was removed, 300 μL of QIAzol was added to the beads, and five volumes were added to the 10% input sample. The beads were vortexed for 2 min to ensure probe detachment and the supernatant was transferred to a new Eppendorf tube. RNA was isolated using the RNeasy Mini Kit with on-column DNAse treatment, according to the manufacturer's instructions (Qiagen).

Sample preparation and UV-crosslinked striatum pull-down

Striata from adult WT mice were collected and placed in an Eppendorf tube containing ice-cold PBS with Ca^{2+} and Mg^{2+} straight after dissection. These were kept in ice until all the remaining striata were harvested. The tissue was then transferred on a culture dish in ice-cold PBS without Ca^{2+} and Mg^{2+} and minced/diced with the help of a scalpel, then transferred to Eppendorf tubes. The minced tissues were centrifuged at 200xg for 5 min at 4°C. The supernatant was removed, and 20 U of pre-warmed papain (Worthington Biochemical Corporation) resuspended in sterile Earle's Balanced Salt Solution (Sigma-Aldrich) were added to each striatum, complemented with 25 μg/mL DNAse I (Sigma-Aldrich) to dissociate the tissues. The tissue was incubated for 45 min at 37°C and 800 RPM. Pre-warmed ovomucoid protease inhibitor (Worthington Biochemical Corporation) was then added to each tissue sample, equal to one-third of the volume of the papain. The smaller pieces of striatum were triturated using a p1000 pipette followed by a p200 or a glass Pasteur pipette attached to a bulb. The tissue was once again centrifuged at 200xg for 5 min. The supernatant was removed, and the pellet was resuspended in 1 mL PBS without Ca^{2+} and Mg^{2+}. The cell suspensions were transferred on a p10 plate on ice and crosslinked at 4000 × 100 μJ/cm^2. The cells were pelleted at 4000 RPM for 5 min. Four pellet volumes of cold MagIC Lysis buffer (ElementZero Biolabs) were added to the cells containing 1X PIC and 5 μM DTT, which were incubated on ice for 10 min. The lysates were centrifuged at 16,000xg for 10 min at 4°C to pellet the insoluble cell components. The cleared cell lysate was then quantified via the Pierce BCA protein assay kit (Thermo Fisher Scientific): approximately 0.9–1 mg of extract was used per probe set (PD-*circDlc1(2)* or PD-SCR, ElementZero Biolabs). 500 μL of MagIC Lysate Dilution Buffer (ElementZero Biolabs) containing 1X PIC and 5 μM DTT was added per mL of cleared lysate. The 10% input fraction was then collected in order to analyze the efficiency of the pull-down procedure. 200 pmol of *circDlc1(2)* or SCR probes were added to the processed lysate. Each sample was placed in a thermo block, shaking at 900 RPM with 3 s on/30 s off cycles, for 30 min at 60°C. The beads then underwent 4 washes with 1 mL of MagIC Wash Buffer I (ElementZero Biolabs), each time shaking at 900 RPM with 3 s on/30 s off cycles, for 10 min at 60°C. A final wash with no incubation was performed with 1 mL Elution buffer (10 mM Tris-HCl, pH 7.5). Beads were finally resuspended in 25 μL of Elution buffer and heated at 92°C for 2 min at 600 RPM. Proteinase K was added to the eluted samples to a final concentration of 2 mg/mL, and incubated for 1 h at 55°C. Five volumes of QIAzol Lysis Reagent were added and RNA was isolated using the RNeasy Mini Kit with on-column DNAse treatment, according to the manufacturer's instructions (Qiagen).

Open field test

Mice were subjected to the open field test in order to assess their exploratory behavior and locomotor activity. Before each behavioral procedure, mice were moved to the room where tests were to be performed and were allowed to acclimatize for 30 min in their home cages. All tests were performed during the light phase. In the open field test, mice were left free to explore an empty Plexiglas arena (40 × 40 × 35 cm) for 30 min. During the test, behavior was recorded using a video camera connected to a video-tracking system (Any-Maze, Stoelting, USA). The distance traveled (m) and the mean speed (m/s) were recorded and used as an index of spontaneous locomotor activity, while the percentage (%) of time spent in the center of the arena was used to assess anxiety-like behavior of the animal, also defined as thigmotaxis. Behavioral stereotypies were additionally assessed during the open field by measuring the grooming time (s) as well as the frequency of leaning and rearing.

Neuromuscular test

On the same day following the open field test, mice underwent neuromuscular tests to assess motor function and muscle strength. The test is based on the latency of the mouse to fall off a metal wire upon exhaustion. Mice were weighed before the test as weight is an affecting factor for the test outcome. Mice were consecutively subjected to two different neuromuscular tests:

- the Hanging Steel test, where the start position of the mouse is with the fore limbs attached to the wire, that is a 30 cm wide 2-mm thick metallic wire secured to two vertical stands.

- the Hanging Wire test, where the start position of the animal is with both fore and hind limbs attached to a metal grid (25 × 20 cm), which will be turned upside down after ensuring that the mouse has a strong grip on it.

In both cases, the wire is maintained 35 cm above a layer of bedding material to prevent injury to the animal when it falls down. During the experiment, the animal's latency time before detaching and falling is measured with a timer and the cut-off for the experiment was 300 s. Mice whose behavior did not match the protocol's standards, such as balancing with their tail or falling off it on purpose, were put back in the starting position.

Contextual fear conditioning (CFC)

After a room habituation time interval of 30 min, mice were subjected to CFC to assess their associative memory. On the first day, mice were placed in the conditioning chamber (Ugo Basile, Varese, Italy) consisting of a transparent plastic cage (21.5 × 21.5 × 35.5 cm) equipped with an infrared camera and a grid floor made of stainless steel rods connected to an electric shock generator. After a 2 min habituation period, five foot-shocks (0.7 mA, 1 s) were delivered through the grid floor at 1 min intervals. Following presentation of the final stimulus, mice remained in the context for 60 s. On the second day, mice were placed in the same context for 5 min without any added stimuli. CFC memory was assessed recording the time spent freezing when there was an absence of movement except for respiratory-related ones.

Calcium imaging recordings and data processing

The AMPA-induced calcium activity was assessed by time lapse recordings on neurons labeled with the high-affinity calcium-sensitive indicator Fluo4-AM (Invitrogen) used at a concentration of 5 μM, which was incubated in the culture medium for 25 min at 37°C. Time lapse fluorescence images were recorded at room temperature through a BX51WI microscope 224 (Objectives: LUMPlanF *N* 10×/0.10, air, and 40x/0.80, water immersion, Olympus 225 Corporation). Fluo4-AM was excited with an Optoscan monochromator (Cairn Research, 226Facersham, UK) at 488 nm using a xenon lamp Optosource (Cairn Research). Neurons were perfused with an HEPES-buffered external solution (NES) containing 140 mM NaCl, 2.8 mM KCl, 2mM $CaCl_2$, 2mM $MgCl_2$, 10mM HEPES, 10 mM D-glucose (pH 7.38 with NaOH; 290 mOsm). A borosilicated glass puffer pipette was filled with 100 μM AMPA (Sigma-Aldrich) and 100 μM cyclothiazide (CTZ, Sigma-Aldrich) (AMPA receptor positive modulator that induces a fast inhibition of AMPAR desensitization) in NES, and moved via an MP-225 micromanipulator (Sutter Instruments, Novato, CA) to reach the core of the field of view, approximately 50 μm over the surface of the dish. Basal fluorescence was assessed for 5 min, then a small volume of agonist-containing solution was puffed on the cells using a pneumatic pico-pump (PV820; World Precision Instruments, Inc., Sarasota, FL) with a short pressure (10 psi; 100 ms). Images were acquired using a CCD CoolSnap MYO camera (Photometrics, Tucson, AZ, USA) and analyzed with the MetaFluor software as fluorescence variation into each region of interest (ROI) corresponding to single cells. To quantify the signal, the formula ΔF (F-F0) was used, where F0 is the mean fluorescence before agonist application and F the fluorescence intensity during the time-lapse acquisition.

QUANTIFICATION AND STATISTICAL ANALYSIS

The standard error mean, the number of biological replicates and the scale bars of the images are indicated in each Figure legend. Statistical tests used to assess significance of differences between means are indicated in each Figure legend. Significance values were depicted in the figures using the following key legend: ns: not significant ($p > 0.05$), *: $p \leq 0.05$, **: $p \leq 0.01$, ***: $p \leq 0.001$, ****: $p \leq 0.0001$. P-values ≤ 0.05 were considered significant. GraphPad Prism was used for statistical test calculation.